An object-based and Lagrangian view on an intense hailstorm day in Switzerland as represented in COSMO-1E ensemble hindcast simulations

Killian P. Brennan[1], Michael Sprenger[1], André Walser[2], Marco Arpagaus[2], and Heini Wernli[1]

[1]Institute for Atmospheric and Climate Science, ETH Zürich, Zurich, Switzerland,
[2]Federal Office of Meteorology and Climatology MeteoSwiss, Zurich, Switzerland

Correspondence: Killian P. Brennan (killian.brennan@env.ethz.ch)

Abstract. On 28 June 2021, Switzerland experienced the passage of several formidable hailstorms, navigating its complex terrain. They unleashed severe hailstones measuring up to $9\,\mathrm{cm}$ in diameter. We present a comprehensive case study to unravel the complex processes involved in the genesis, intensification, and dissipation of this impactful weather event. To this end, we investigate ensemble hindcast simulations using the COSMO-1E numerical weather prediction model that includes the

5 HAILCAST hail growth parameterization. A tracking algorithm is introduced that facilitates the object-based analysis of the simulated hailstorms, addressing the inherent challenges of tracking hailstorms within numerical simulation outputs. By scrutinizing the storm's evolution across various phases, particularly during intensification, the study conducts a storm-relative analysis of 100 hailstorms simulated on this day by the 11-member ensemble with lifetimes of $>2.5\,\mathrm{h}$. Furthermore, the investigation utilizes Lagrangian air parcel trajectories initiated along the hail track to analyze the inflow of air sustaining the

10 storm updraft. This exploration provides fresh insights into the low-level flow patterns and moisture sources contributing to the storm's vigor, and it reveals the importance of topography for the various stages of the storms. The most important findings from this detailed hailstorm investigation are (i) COSMO-1E with HAILCAST produces realistic storm tracks and lifespans that are in good agreement with radar observations, (ii) intricate storm structures are resolved in the simulations and reveal hail fall followed by precipitation, and (iii) Lagrangian trajectories show that inflowing air can be drawn across the main Alpine

15 crest and experiences rain before reaching saturation conditions in the storm.

1 Introduction

Severe convective storms offer some of the most intense and impressive weather on our planet. Hailstorms dramatically display the forces of nature at play inside so-called supercells. Supercell thunderstorms are a distinct form of cumulus structure, representing the most severe category of thunderstorms (Schmid et al., 1997; Markowski and Richardson, 2010; Bluestein,

20 2013; Houze, 2014). Unlike their counterparts, i.e., single and multi-cell storms, supercells are relatively rare but notorious for generating the most intense hailstorms and powerful tornadoes (Graf et al., 2011). Distinguished by their towering vertical reach spanning the troposphere and expansive horizontal spread extending over several tens of kilometers, supercells surpass the typical scale of single-cell storms. Within them, a singular storm-scale circulation dominates (Markowski and Richardson,

2010; Houze, 2014). Thunderstorms with strong enough updrafts can form hail, as hail embryos collect mass when they are
25 lofted into the region with supercooled liquid water from the storm by strong updrafts (Pruppacher and Klett, 2010; Allen et al.,
2020). Hail ranks among the costliest atmospheric phenomena at mid-latitudes (Changnon, 1999; Crompton and McAneney,
2008). In Switzerland, hailstorms are a frequent phenomenon during the convective season (Houze et al., 1993; Nisi et al.,
2016), causing extensive damage to agriculture, buildings, and cars (BAFU, 2016). Summer 2021 was the most active hail sea-
son in Swiss records, resulting in various studies that collected and analyzed radar, hail sensor, and crowd-sourced observations
30 (Kopp et al., 2022), measured the hail size distribution by drone (Lainer et al., 2024), while other studies modeled hail damage
to agriculture and infrastructure in this season (Portmann et al., 2023; Schmid et al., 2024). The number of days with hail in
Switzerland has increased significantly in the last 50 years (Wilhelm et al., 2024), further highlighting the importance of hail
research in this region.

The potential for extensive damage illustrates the need to improve forecasts of hailstorms and advance our understanding
35 of the meteorological processes associated with hailstorms. Using parameters or proxies such as convective available potential
energy (CAPE), vertical wind shear, and storm-relative helicity (SRH), predictions about the probability of occurrence and
intensity of convective storms can be made (i.e. Ulbrich and Atlas, 1982; Marcos et al., 2021). Short-term predictions of hail
are currently conducted using radar-based nowcasting, where the future state of severe weather objects such as hailstorms
is extrapolated from current radar observations and movement vectors of convective cells (e.g. Hering et al., 2004; Trefalt
40 et al., 2023). Predictions with lead times beyond $3\,\mathrm{h}$ must rely on numerical weather prediction (NWP) models (e.g. Sun
et al., 2014). In addition to radar-based investigations, high-resolution numerical weather prediction models with explicitly
simulated deep convection allow novel insights into the physics of convective storms. As there is inherent uncertainty in the
prediction of atmospheric processes (Lorenz, 1963) and especially the position and intensity of mesoscale storms, ensemble
models were developed to address this issue and assess the uncertainty of forecasts. An ensemble simulation consists of several
45 members that are each initiated with slightly different initial conditions and, during model integration, employ stochastically
perturbed parametrization tendencies. These small perturbations diverge throughout the model run and the resulting spread of
the physically consistent forecasts is a measure of the overall forecast uncertainty (Palmer and Hagedorn, 2006).

The challenges in predicting hail stem from two main factors: hail formation occurs within intense convective storms, where
the prediction of the time and location of the convective triggering, as well as the resulting intensity, is influenced by complex
50 mesoscale processes (e.g., Ducrocq et al., 2008; Barthlott and Kalthoff, 2011; Barthlott and Barrett, 2020). Additionally, the
microphysical processes governing hail formation are intricate and not adequately represented in most operational microphysics
parameterization schemes (e.g., Adams-Selin and Ziegler, 2016; Brimelow, 2018; Allen et al., 2020). An effective strategy to
tackle these challenges is to conduct high-resolution ensemble forecasts (Sect. 2.1) and diagnose the occurrence of hail with a
suitable parameterization scheme (Sect. 2.1.1).

55 In this study, we utilize a single convection-permitting ensemble hindcast simulation, performed with the model COSMO-1E
(Klasa et al., 2018), to examine a hail day that severely impacted Switzerland in the summer of 2021. Hail formation is not
explicitly simulated, as done in previous studies using the COSMO model with an extended cloud microphysics parameteri-
zation including a hail category (e.g., Seifert and Beheng, 2006; Noppel et al., 2010), but instead hail formation is diagnosed

during model integration using the HAILCAST parameterization (Adams-Selin and Ziegler, 2016; Adams-Selin et al., 2019),
60   see Sect. 2.1.1. With this case study we contribute to the body of literature on severe weather events in Central Europe and
beyond, making use of a high-resolution ensemble simulation and sophisticated diagnostics. Several earlier studies (Schiesser
et al., 1995; Trefalt et al., 2018; Rigo et al., 2022; Bechis et al., 2022) analyzed severe hailstorms in complex topography based
on radar observations. Barras et al. (2021) investigated the temporal clustering of hail days in Switzerland and Mohr et al.
(2020) considered the role of large-scale dynamics in a sequence of severe thunderstorms in Europe. The specific objectives
65   of our ensemble simulation-based investigation are to (i) explore the physical processes and environmental conditions driving
the storm's initiation, intensification, and dissipation, (ii) analyze the low-level inflow of air into the hailstorm and the evo-
lution throughout its life cycle, and (iii) assess the influence of topography on storm development. The use of the ensemble
simulations provides us with a larger set of physically consistent storm tracks (compared to single deterministic simulations),
enabling a more robust interpretation of the relevant physical processes.

70   Previous studies have investigated atmospheric parameters and environments that influence hailstone size. Analysis in these
studies is generally based on observational data on hail in a given region and analysis of reanalysis data in that same region (e.g.
Taszarek et al., 2017, 2020; Zhou et al., 2021; Calvo-Sancho et al., 2022). A similar analysis can be performed in convection-
resolving NWP models, where the environment is assessed in the immediate vicinity of a storm as it moves through the domain
(e.g. Prein and Heymsfield, 2020; Lin and Kumjian, 2022). Furthermore, rather than investigating the Eulerian neighborhood
75   of a convective storm, Lagrangian backward trajectories can be employed to specifically investigate the origin of air feeding
the storm updraft, as shown in recent publications, where the low-level inflow and vorticity sources of supercells in idealized
simulations were investigated in the Lagrangian framework (Gowan et al., 2021; Coffer et al., 2023). In addition to an Eulerian
framework of analyzing atmospheric processes, such a combined object-based and Lagrangian approach – e.g., by investi-
gating backward trajectories from the core updraft region along simulated storm tracks – offers complementary insights into
80   mechanisms at play inside storms. Technically, such an approach therefore requires a specific tracking algorithm for tracking
hailstorms in high-resolution simulation output, and a trajectory tool to study the airflow through the core updraft regions. For
the latter, we use an established trajectory tool, whereas, for the former, we introduce a storm tracking scheme specifically
developed for our high-resolution model output (see Sect. 2).

A brief discussion of the synoptic situation introduces the case study (Sect. 3.1), followed by a description of the storm tracks
85   (Sect. 3.2). The storm-centered perspective is then applied to investigate the spatial and temporal structure of a selected storm
and a composite of all long-lived storms simulated by the ensemble in the case study period (Sect. 4). In Sect. 5, the inflow of
air into the storm and its implications for the storm's evolution are investigated. Furthermore, the role of topographical features
in influencing the various stages of the storms will be examined (Sect. 4). Overall, the study revolves around unraveling the
complexities of hailstorm development, providing insights into the storm's life cycle, and improving our understanding of
90   hailstorms in numerical weather simulations.

2 Methods and data

This section introduces the data and methods used in this study. The numerical weather model COSMO-1E and the HAILCAST parameterization for hail diameter on the ground are described in Sect. 2.1 and Sect. 2.1.1, respectively. The tracking algorithm used to identify and track the storms in the COSMO-1E simulations is described in Sect. 2.2. The ECMWF global ERA5 reanalysis (Hersbach et al., 2020) was used in this study to characterize the large-scale atmospheric conditions.

2.1 COSMO simulations

The COSMO model is a non-hydrostatic limited-area NWP model. The governing equations describing compressible flow in a moist atmosphere are solved on a rotated-pole-structured grid with hybrid terrain-following height coordinates (Steppeler et al., 2003). Although designed and optimized for operational NWP, the COSMO model is also extensively utilized in scientific applications on the meso-β and meso-γ scale. The COSMO model is most suitable for forecasts at a convection-resolving scale (Baldauf et al., 2011). Parameterizations represent unresolved subgrid-scale physical processes, including a bulk microphysics scheme with five species (cloud water, cloud ice, rain, snow, and graupel) and schemes for shallow convection, boundary layer turbulence, radiation, and land-surface processes. Note that hail is not explicitly simulated as a species in the microphysical parameterization but is calculated diagnostically (Sect. 2.1.1).

COSMO-1E is the operational ensemble model used at MeteoSwiss (Klasa et al., 2018, 2019). COSMO-1E features 11 ensemble members, which are calculated every $3\,\mathrm{h}$ for the next $33\,\mathrm{h}$. The ensemble members have varying initial and boundary conditions, as well as stochastically perturbed parameterization tendencies. The horizontal grid size is $1.1\,\mathrm{km}$ with 1170×786 grid-points, covering the entire Alpine region (Fig. 1a). Vertically it extends through 80 model layers to an altitude of $22\,\mathrm{km}$. The model runs with a time step of $10\,\mathrm{s}$, and atmospheric fields relevant to our application are written to disk every $5\,\mathrm{min}$. For this study, a COSMO-1E ensemble hindcast was initialized at 06:00 UTC on 28 June 2021 in its operational setup, just with more frequent output. The simulation output amounts to $\approx 17\,\mathrm{TB}$ of data.

2.1.1 HAILCAST

HAILCAST is a diagnostic, physics-based hail growth parameterization. It consists of a one-dimensional, steady-state cloud model which is coupled with a time-dependent hail growth model (Brimelow et al. (2002); Brimelow (1999); Jewell and Brimelow (2009), based on Poolman (1992)). HAILCAST estimates hail size (maximum, mean, and standard deviation of the diameter) expected at the ground. It is designed to be embedded in a convection-resolving atmospheric model. Hailstone growth is modeled through liquid water accretion, ice particle collection, condensation, and sublimation. The hailstone temperature is explicitly calculated, determining wet and dry growth regimes. As HAILCAST is a one-dimensional model, horizontal advection of hailstones is not accounted for. Multiple initial embryo sizes are injected into the updraft and their size is tracked along their vertical path through the convective cell. However, for this study, only the hail size yielded by the largest, $10\,\mathrm{mm}$ embryo was considered. In addition, HAILCAST features include variable hail density, rime soaking, temperature-dependent

ice collection efficiency, liquid water shedding, and enhanced melting during collision with $> 0\,°C$ water (Adams-Selin and Ziegler, 2016).

2.2 Storm tracking algorithm

125 Hailstorms can be relatively small atmospheric features that may move at high velocities, which poses a complication to tracking tools, as such features might not overlap spatially between two model output time steps. In the tracking algorithm used in this study, hailstorms are identified as two-dimensional objects formed by grid-points where a parameter (e.g., max. hail size) exceeds a certain threshold. An adaptive threshold allows small, high-intensity storms to be separated in a larger, mesoscale convective system. Further, an adaptive threshold allows storms to be tracked in their developing, mature, and

130 dissipating stages, which might have very different intensities.

There are several approaches to tracking atmospheric objects such as convective storms and other atmospheric phenomena described in the literature (e.g. Neu et al., 2013; Gropp and Davenport, 2021; Meredith et al., 2023; Liu et al., 2024). Recent studies (Schär et al., 2020; Rüdisühli, 2018; Rüdisühli et al., 2020; Schemm et al., 2020) described an on-the-fly feature tracking algorithm, based on overlapping areas of the features identified at the previous and current time steps. Importantly,

135 as such algorithms run online (that is, during model run-time), it can benefit from a very high temporal data resolution, and simply using overlapping areas is enough to track features. For data with less temporal resolution, a simple overlap association is not sufficient for small, fast-moving objects. This shortfall can be combated by implementing dynamical tracking, where the search area at a given time step is not just taken from the location of the tracked feature at the previous time step, but informed by previous feature movement. An approach to using horizontal wind fields at multiple model levels to guide the

140 search area in the next time step was implemented in Purr et al. (2019), allowing tracking in lower time resolutions. However, their algorithm does not account for the splitting and merging of storms and is reliant on wind fields being available during tracking. TRT (Thunderstorms Radar Tracking, Hering et al. (2004); Trefalt et al. (2023)), a radar-based tool for thunderstorms nowcasting that is used operationally by MeteoSwiss, is another tracking algorithm that does not account for splitting and merging but has an adaptive threshold implementation. Because it benefits from the high temporal resolution of $2.5\,min$ for

145 the radar volume scans, it does not require dynamical tracking. TRT has been further developed (Thunderstorm Detection and Tracking (T-DaTing); Feldmann et al., 2021), adding simple two-way splitting & merging support and optical flow to predict storm movement.

None of the existing tracking implementations fulfill all of the tracking requirements needed for our application, such as dynamical tracking, adaptive threshold, and accounting of splitting and merging. We therefore present a novel tool developed

150 to identify and track features associated with convective storms. It is optimized to track small, fast-moving objects in two-dimensional fields of limited-area atmospheric model simulations with high temporal and spatial resolution. In essence, the algorithm detects objects with a corresponding mask based on various filtering criteria, such as area, intensity, and distance, and uses the last known object propagation vector to inform the search area during the next tracking time step. The tracking algorithm also accounts for splitting and merging objects and can solve complex scenarios involving multiple objects with non-

155 trivial evolution pathways. For a detailed description of the tracking algorithm, please refer to Appendix A. In the following,

only tracking parameters and details specific to this study are listed. The tracking was performed for updrafts identified in the vertical wind field w on model level 25, which corresponds to an average altitude of $z = 7.5 \, \mathrm{km}$, or pressure of $400 \, \mathrm{hPa}$. Features with $w > 5 \, \mathrm{m \, s^{-1}}$ were tracked, while features with a prominence exceeding $20 \, \mathrm{m \, s^{-1}}$ and with maxima separated by more than 10 grid-points were divided using a watershed algorithm. The area threshold was set to 5 grid-points, while the storm mask was inflated by 4 grid-points using binary dilation, which applies a circular disk kernel to the storm mask to expand the borders of the mask.

3 Overview of case study

The selection of the case study date can be justified by the extensive damages that occurred on 28 June 2021. Large areas of the Swiss plateau were impacted by damaging hail, while hailstones with diameters in excess of $9 \, \mathrm{cm}$ wreaked havoc in select villages in the Alpine foothills. In fact, the largest area within Switzerland covered by severe hail since 2002 was recorded on this day, with return periods locally exceeding $100 \, \mathrm{years}$ (Kopp et al., 2022). More than $10\,000$ crowd-sourced reports were collected on that day, which represents the highest daily number on record. At the time, reports collected in June and July 2021 accounted for half of all reports collected since the introduction of the reporting function more than 5 years earlier (Kopp et al., 2022). Insured building damage in 4 cantons alone accounts for more than 400 million Swiss Francs (CHF), with more than 1000 heavily damaged buildings with $> 100\,000$ CHF damage each (Schmid et al., 2024).

3.1 Synoptic situation

On 28 June 2021, analysis of the upper-level flow situation over western and central Europe reveals a prominent potential vorticity (PV) cutoff over western France (Fig. 1a). It moved eastwards from the French Atlantic coast towards the main Alpine crest, and thereby brought a cold air anomaly aloft while advecting warm and moisture-laden Mediterranean air towards the Swiss plateau at low levels. The PV cutoff originated from a PV streamer over the British Isles that formed four days earlier. Besides the presence of a shallow surface cyclone over north-western France, the pressure distribution across central Europe was flat. In Switzerland, T_{2m} approached $30 \, ^\circ \mathrm{C}$ in the pre-storm environment, with dew-point temperature around $20 \, ^\circ \mathrm{C}$. Widespread CAPE $> 2000 \, \mathrm{J \, kg^{-1}}$ as well as some CIN were present throughout the domain, accompanied by 0-6 km directional shear larger than $25 \, \mathrm{m \, s^{-1}}$, yielding an atmosphere primed for organized convection (Fig. 1b). The vertical profile also reveals a high level of moisture throughout the hail growth layer (HGL, extending from $0 \, ^\circ \mathrm{C}$ to $-38 \, ^\circ \mathrm{C}$ levels). It should be noted that the HGL is even moister in the measured balloon sounding from Payerne at 12:00 UTC (not shown). The measured profile also features a more pronounced low-level inversion than the simulated profile. This inversion inhibits the premature destruction of CAPE through unorganized convection and allows for further accumulation of heat and moisture in the boundary layer throughout the day. As a result, an intense and long-lived mesoscale convective system originating in western Switzerland moved along the main Alpine crest in a north-easterly direction throughout the day, as further discussed below. More details about the weather situation on this day can be found in Kopp et al. (2022).
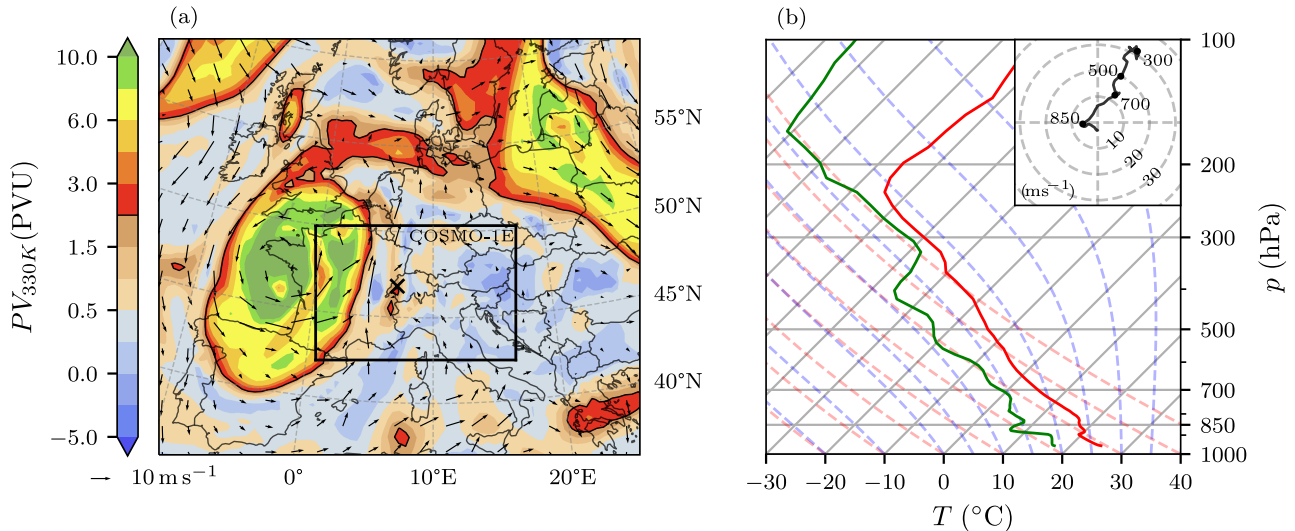
Figure 1. Synoptic situation at 12:00 UTC on 28 June 2021. (**a**) Potential vorticity on the $300\,\mathrm{K}$ isentrope (colors, in PVU; the black contour denotes the dynamical tropopause at $2\,\mathrm{PVU}$), the quivers show horizontal wind at $850\,\mathrm{hPa}$, based on ERA5. The $\times$ marker locates the position of Payerne. The COSMO-1E domain is also delineated (black rectangle). (**b**) Skew-T Log-P diagram of the vertical profile in Payerne (from COSMO-1E, member 0). The ambient temperature and dew point profiles are shown in red and green solid lines, respectively, while the red and blue dashed lines represent the dry and moist adiabats. The hodograph displays the u and v wind components from the surface to $200\,\mathrm{hPa}$.

3.2 Storm tracks

Storm tracks were determined in all ensemble members using the algorithm described in Sect. 2.2. Although there are 6611 storm tracks across all members with a lifespan $> 15\,\mathrm{min}$, only 124 storms have a lifespan $> 2.5\,\mathrm{h}$, of which 100 storms feature
190 updraft velocities $> 25\,\mathrm{m\,s^{-1}}$ at $400\,\mathrm{hPa}$. Storm lifespans and maximum storm area both follow a log-normal distribution. The ensemble members are generally well in agreement in terms of the produced storm lifetimes and areas, although the ensemble spread is larger at the tails of the distribution (Fig. 2). The distribution of the simulated storm lifespans aligns very well with the observed storm tracks from the radar. However, here it must be kept in mind that for the observations and the simulation, two different tracking algorithms on two different fields were used and thus direct comparisons are only meaningful to a limited
195 extent. For bins of life expectancy below $1\,\mathrm{h}$, the ensemble spread, although narrow, contains the observed lifespan prevalence. The number of longer-lived storms with lifespans $> 2\,\mathrm{h}$ is underestimated by a factor of ≈ 2. The agreement between the simulated and observed storm areas is lower, especially with respect to the smallest storm areas (Fig. 2b).

Although most of the long-lived tracks are centered on the Napf region (47°N, 8°E, Fig. 3), there are also some isolated tracks upstream and downstream of this region. Interestingly almost all simulated storms occur north of the Alpine crest.
200 Compared to the measured tracks, the simulation misses some of the South-Alpine storms, while overproducing storms further
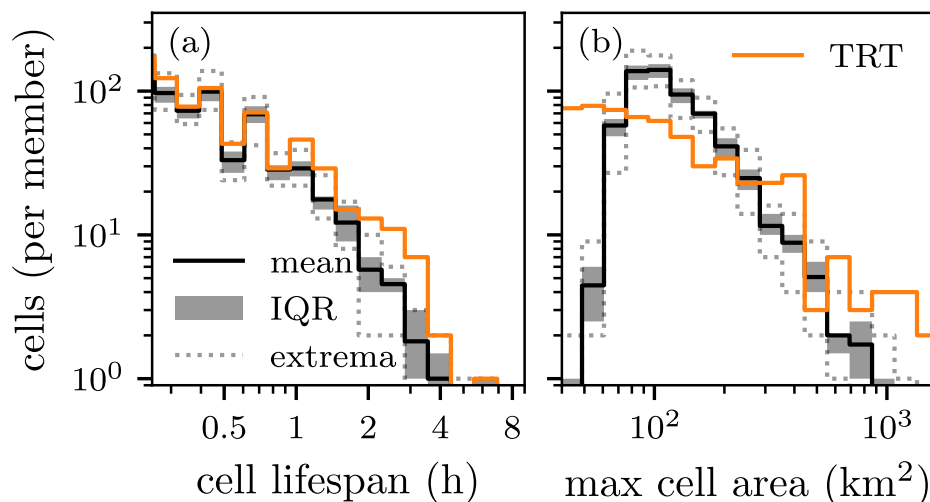
Figure 2. Distributions of **(a)** storm lifespan, and **(b)** maximum storm area reached throughout the life cycle, with ensemble mean (black line), interquartile ranges (IQR, gray shading), and respective extrema (gray dashed) from the COSMO-1E simulation. Orange lines indicate the values for the radar-observed storm tracks on the case study day.

downstream in the Black Forest region. But overall, focusing on the severe hail event in northern Switzerland, this analysis has shown that the characteristics of the simulated storm tracks are comparable to the measured tracks on the case study day.

Next, we consider a subset of all storm tracks to be investigated in detail in Sections 4 and 5. Specifically, $2.5\,\text{h}$ was the selected storm lifespan threshold for a detailed analysis of the storm inflow and structure, using storm-centered and Lagrangian perspectives. This lifespan threshold gives a good compromise of long enough lifespans to investigate the storm's life cycle while still allowing for robust statistics thanks to the use of an ensemble simulation. Furthermore, only long-lived storms that achieved updraft velocities greater than $25\,\text{m s}^{-1}$ at least once within their lifetime were considered. Although the storms selected using these criteria only account for 1.7% of the tracked storms, 12.6% of the storms that exhibit $w >25\,\text{m s}^{-1}$ within their evolution feature lifespans $>2.5\,\text{h}$, meaning that the investigation of long-lived storms favorably covers intense storms. To facilitate the investigation of storm initiation, the initial time step of each storm is extrapolated backward in time by $0.5\,\text{h}$ using the mean lifetime storm propagation vector.

For more detailed analyses of an individual hail cell in Sect. 4 and Sect. 5, one exemplary storm was selected from ensemble member 5, which shows a similar realization to the actual storm that moved across central Switzerland and was discussed in detail in Kopp et al. (2022) (Fig. 3). This storm produced maximum hail diameters of $48.4\,\text{mm}$ according to HAILCAST.

In this study, the storm tracks are used to enable a storm-centered view of the convective environment (Sect. 4) and initialize Lagrangian trajectories along the tracks (Sect. 5).
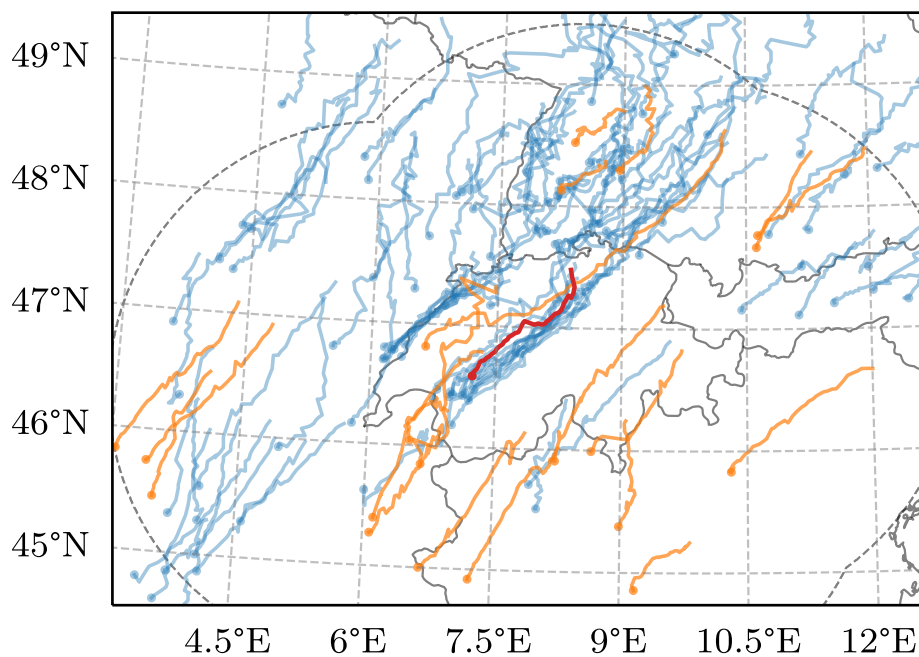
Figure 3. Overview of tracked storms with lifespans greater than $2.5\,h$ that reach updraft velocities $> 25\,\mathrm{m\,s^{-1}}$ from all COSMO-1E members (blue). The start of storm tracks is marked with a dot, while the storm selected to be investigated in detail is highlighted in red. Orange tracks indicate the radar-observed tracks on the case study day with lifespans $> 2.5\,h$ as classified by TRT. The dashed line denotes the extent of the radar domain.

4 Storm-centered perspective

In this section, we explore a storm-centered perspective. To this end, key environmental variables are determined along storm tracks, including various thermodynamic and dynamic parameters, such as near surface potential temperature, specific humidity, CAPE and CIN, vertical wind shear, and vertical vorticity. More specifically, a 50×50 grid-point box of all relevant variables centered at the storm location is extracted along the track of the investigated storms. Subsequently, the spatial structure of a hailstorm and its temporal development can be analyzed along its track, and atmospheric fields from multiple storms can be composited to arrive at an idealized representation of a hailstorm as simulated by the model on this particular day.

4.1 An illustrative example

As an illustrative example, we investigate the selected storm as described in Sect. 3.2.

The storm exhibits two distinct phases, as is evident from the evolution of the vertical wind profile along the track (Fig. 4a). After initiation of deep convection at 12:00 UTC from preexisting shallow convection, a latent phase lasts for $1\,h$, during which maxima vertical wind velocities are restrained to $20.5\,\mathrm{m\,s^{-1}}$. Then, a first intensification (13:00—13:30 UTC) follows, when

the vertical velocities increase to $31.0\,\mathrm{m\,s^{-1}}$. The start of this transition coincides well with the drop in topographical height
230 from about 1300 to $800\,\mathrm{m}$ experienced by the storm at 13:00 UTC (Fig. 4c). Such a rapid drop in topographical height would
give the storm immediate access to warmer and moister air, which in turn would fuel the storm's intensification. Preceding the
most intense phase of the storm, a period of rapid intensification in updraft velocities (13:30—14:30 UTC) coincides with a
clear increase of maximum low level ($900\,\mathrm{hPa}$) Θ_e values from $341.9\,\mathrm{K}$ to $346.6\,\mathrm{K}$ (Fig. 4d). Notably, hail diameter exhibits
a less rapid increase than the vertical wind (Fig. 4f). There is also a phase with lower values for w and q_c prior to the most
235 intense phase, for which no suitable explanation has been found (13:20—14:00 UTC). The maximum vertical velocity occurs
at 14:40 UTC with values reaching $52.6\,\mathrm{m\,s^{-1}}$ and hail diameters of $48.4\,\mathrm{mm}$ (Fig. 4f). This peak in intensity is mirrored in
the mid-level cloud water content (Fig. 4b). The maximum precipitation intensity produced by this storm during $5\,\mathrm{min}$ was
$441\,\mathrm{mm\,h^{-1}}$.

The evolution of convective environment parameters is discussed in the following. Maxima in $0-6\,\mathrm{km}$ vertical wind shear
240 (not shown) and CAPE lead the updraft maxima by an offset of 0.5 and $1\,\mathrm{h}$ respectively (Fig. 4e). The hail diameter maxima
reached throughout the storm lifetime coincide with the most intense phase; however, the decay in d_{hail} is not as swift as the
decay in intensity as given by the vertical wind (Fig. 4a). In this case, the relation between the maximum and mean values of
hail diameters reported by HAILCAST within the storm environment is constant throughout the storm life.

4.2 Composite hailstorm structure

245 Next, in order to gain more statistically robust insight into the structure of the archetypal hailstorm in the simulations, compos-
ites of the selected storms were calculated. To this end, atmospheric fields from a 50×50 grid-point box centered along the
storm track were collected from all storms with lifetimes $> 2.5\,\mathrm{h}$ at time steps with $w > 25\,\mathrm{m\,s^{-1}}$, in order to investigate the
storm structure during the mature phase. From the mean fields emerges the idealized structure of a storm environment. In the
following, vertical cross-sections and horizontal views of various variables are presented.

250 First we consider the vertical cross-section of the storm-centered composites (Fig. 5). Contours of $0.1\,\mathrm{g\,kg^{-1}}$ cloud water
and ice content (chosen as the threshold for visible clouds) reveal intricate cloud structures. A low cloud base extending
down to $\approx 850\,\mathrm{hPa}$ can be distinguished in front of the rain shaft. The anvil of cloud ice precedes the slanted updraft column
by more than $25\,\mathrm{km}$. Impressive composite mean updraft velocities of $16.7\,\mathrm{m\,s^{-1}}$ lead to an overshooting top protruding
into the stratosphere. This overshooting top can be identified in both the mixing ratios and in the compressed isentropes
255 (Fig. 5b). Judging by the vertical separation of isentropes near the ground, the atmosphere's stability increased after the storm
passed. Interestingly, cloud water directly in the updraft column only converts to cloud ice and precipitation species as it
reaches the $-38\,^\circ\mathrm{C}$ level. This is evident from the region of cloud ice larger than $0.1\,\mathrm{g\,kg^{-1}}$, which only marginally extends
downwards from temperatures above $-38\,^\circ\mathrm{C}$. At temperatures above $-38\,^\circ\mathrm{C}$, water droplets can only freeze heterogeneously,
meaning they require an ice nucleating particle to initiate freezing, while at temperatures below $-38\,^\circ\mathrm{C}$, water droplets will
260 freeze homogeneously, without the aid of an ice-active particle. Whether this hints toward model limitations or is physically
plausible would need to be investigated further. The microphysics parameterizations may not be ideally suited for such extreme
updraft velocities, and freezing that occurs only homogeneously is an indication of this hypothesis, as heterogeneous freezing
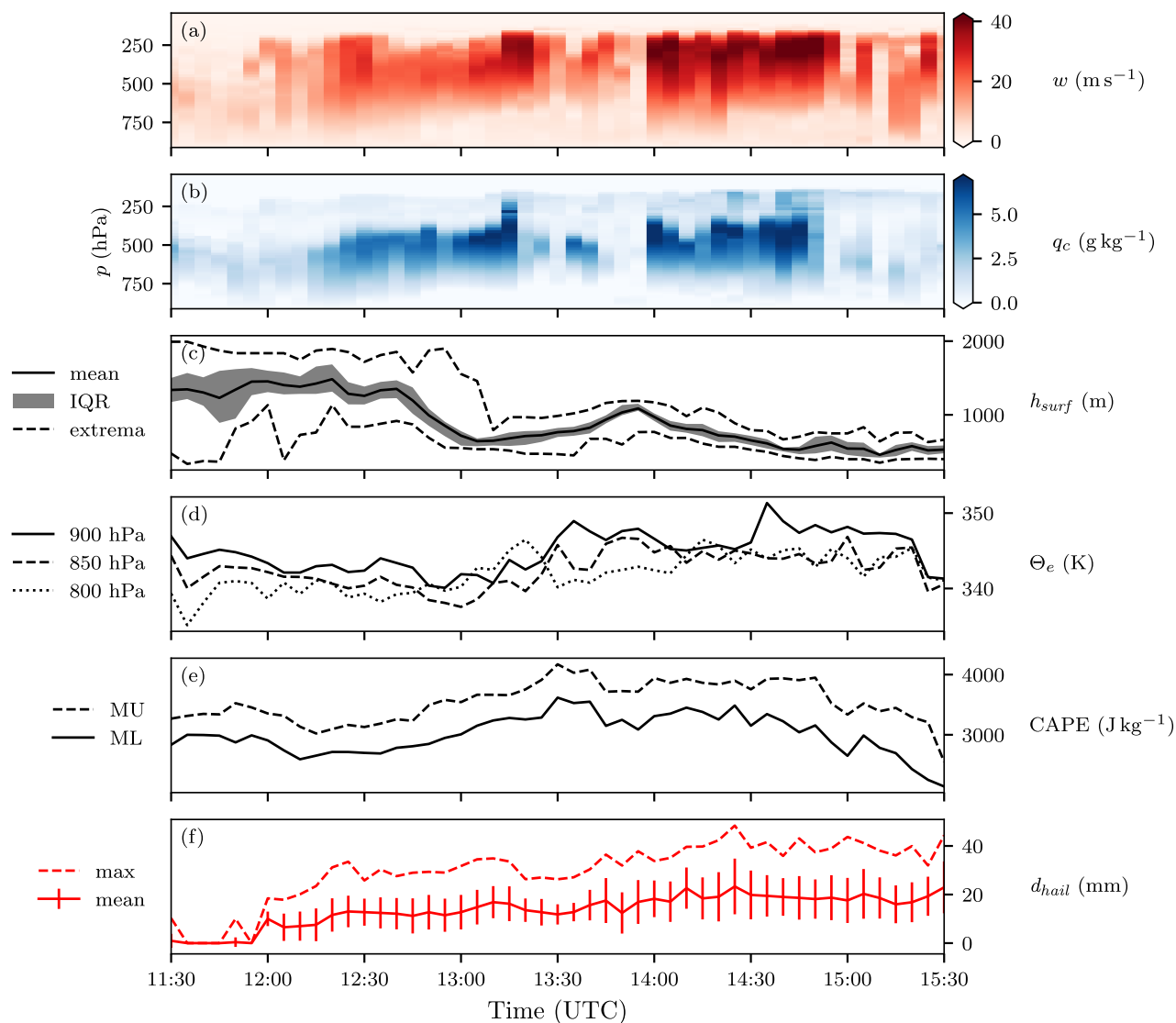
Figure 4. Temporal evolution of a selection of storm-centered variables (within the 50×50 grid-point box) along the red storm track in Fig. 3. The horizontal maxima of the respective variables are shown as colored pixels for the 3D variables (**a**) vertical velocity w, and (**b**) cloud water content q_c. (**c**) shows the distribution of topographical height within the storm mask, (**d**) and (**e**) the maximum values of Θ_e and CAPE, respectively. (**f**) shows the maximum and mean hail diameter values within the storm as reported by HAILCAST, with the standard deviation indicated by error bars. All values from COSMO-1E simulation.

initiated by ice nucleating particles is generally considered the predominant freezing pathway (Pruppacher and Klett, 2010, and references therein). Negative vertical movement only shows up in a few regions in the composite, near the ground and just behind the rain shaft. This points towards the possibility of large-scale subsidence as a process for balancing the storm

265
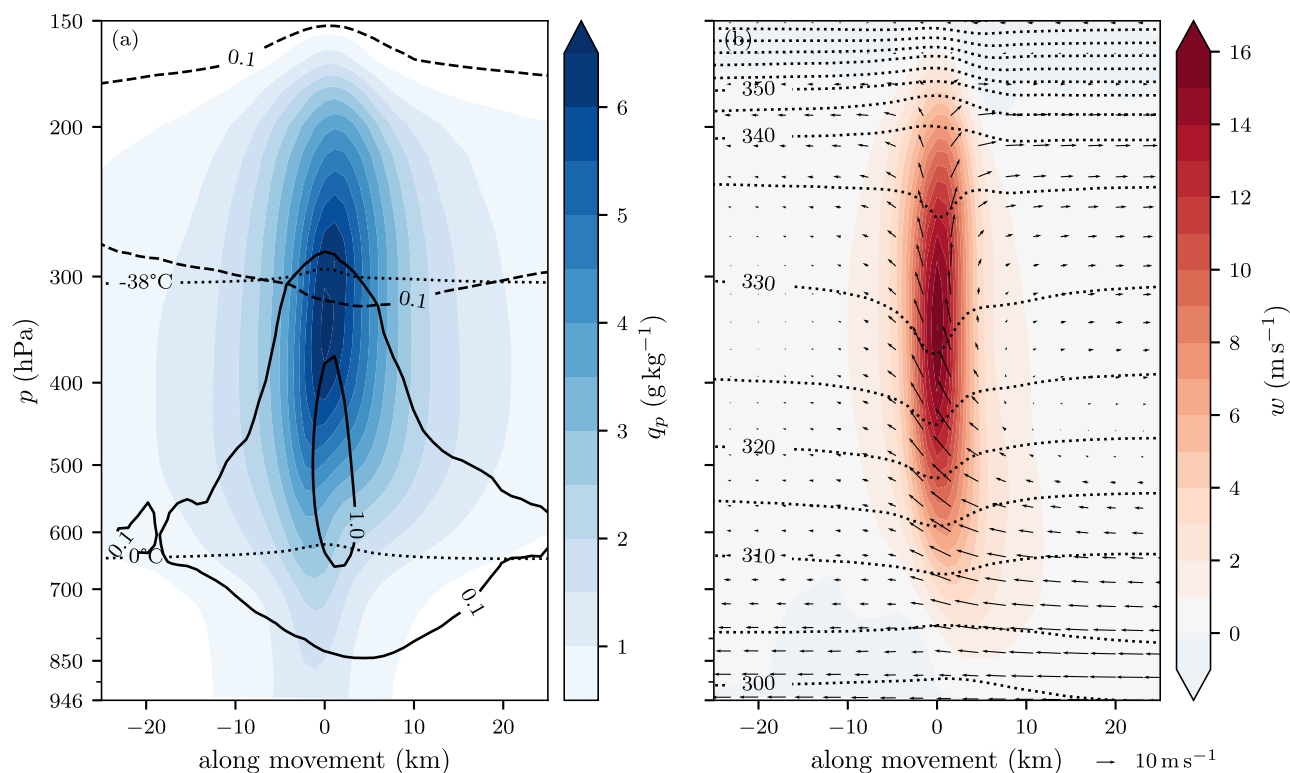
Figure 5. Vertical cross-section along the propagation direction of the storm-centered composite of $n = 100$ storms with lifespans $> 2.5\,\mathrm{h}$ at time steps with $w > 25\,\mathrm{m\,s^{-1}}$, identified in all COSMO-1E ensemble members. The storm is moving to the right and the center ($0\,\mathrm{km}$) represents the storm track center. (**a**) Filled contours denote the total hydrometeor mixing ratio, solid and dashed contours represent cloud water and cloud ice mixing ratios $(\mathrm{g\,kg^{-1}})$, respectively, while the $0\,^{\circ}\mathrm{C}$ and $-38\,^{\circ}\mathrm{C}$ levels are shown as dotted lines. (**b**) Vertical wind field (in $\mathrm{m\,s^{-1}}$, filled contours), isentropes (in K, dotted contours), and in-plane, storm-relative wind vectors, quivers.

updrafts, rather than localized precipitation-associated downdrafts. However, it also needs to be mentioned that the composites are centered on the positive updraft maxima, which therefore are well aligned by design, whereas the downdrafts might have slightly different locations for each storm and might cancel out when calculating the mean. Additional features that are more variable and therefore less well captured by the composite but present in individual cross-sections include detailed shelf and wall clouds extending almost down to the ground. A selected example of such features are shown in the Appendix (Fig. D1).

Next, we examine the horizontal structure of the storm-centered composites (Fig. 6). The potential temperature field at the ground shows a strong gradient ($3\,\mathrm{K}$ within $25\,\mathrm{km}$), offset $60°$ from the storm movement direction, with a minimum located just behind the hail shaft. This minimum coincides with the pressure maximum. Both extrema are caused by the downdraft air entrained by intense precipitation and evaporative cooling. The wind vector field also displays near-ground divergence at this exact location, where the downdraft translates into the horizontal wind at the surface. $20\,\mathrm{km}$ ahead of the storm, an area of

12

convergence can be observed in the $10\,\mathrm{m}$ wind field. The location of near-surface convergence of the horizontal wind denotes the beginning of the updraft column. Just in front of the storm center, the gust front can be determined by the near-ground composite mean wind velocity maximum of $3.3\,\mathrm{m\,s^{-1}}$ (Fig. 6a). At the inflow level, which is located around $850\,\mathrm{hPa}$ (Sect. 5), a specific humidity maximum can be found where the air converges with a cyclonic component in the horizontal wind field.

280 At this level, the water vapour content of the air reaches on average values of $10.6\,\mathrm{g\,kg^{-1}}$ (Fig. 6b). Higher up, at $400\,\mathrm{hPa}$ where the updraft core is located (Fig. 5b), the near-storm horizontal winds are governed by the synoptic situation, i.e., largely determined by the pressure gradient and mostly unaffected by the presence of the storm. On average, the updraft core of the storm at this level is no more than $10\,\mathrm{km}$ across (Fig. 6c). As the tracking of the storms is also performed at this level and on the vertical wind, the centers of the respective vertical wind maxima are well aligned and thus the resulting composite yields a

285 very defined structure. Lagging behind the storm center by about $5\,\mathrm{km}$ the maximum in rain rate can be found, reaching mean values of $30\,\mathrm{mm\,h^{-1}}$. The footprint of the liquid precipitation is slightly asymmetric, extending further to the left, relative to the mean storm motion. The cloud water outline, in contrast, has a slight lead on the center of the storm, which is due to the tilted updraft (Fig. 6d). Compared to the rain, the hail maxima is much more aligned with the center of the storm. Co-location of the hail and updraft maxima is to be expected, as HAILCAST does not account for horizontal advection of hail stones. In contrast,

290 since graupel is explicitly included in the COSMO microphysics, it is subject to horizontal advection in the simulations. Only a small offset of the graupel maximum from the storm center exists (Fig. 6e). The location of graupel gives an upper bound on the potential advection of hail, as graupel has a smaller terminal velocity than even the smallest hailstones, giving more time for horizontal advection to take effect.

CAPE values rapidly decrease as the storm approaches. $25\,\mathrm{km}$ in front of the storm, CAPE values are on average $1600\,\mathrm{J/kg}$,

295 while they fall below $600\,\mathrm{J/kg}$ just as the storm passes. The thunderstorm anvil cloud extends well beyond the window size of $25\,\mathrm{km}$ in front of the storm (Fig. 6f). Liquid precipitation following a hail event can be an important consideration for the damage caused by a storm, as rain can enter into buildings through hail-damaged skylights, windows and roofing causing further damage through water ingress (Ridder et al., 2020). Our analysis shows that, on average, liquid precipitation immediately followed hail fall during the passage of the storms (Fig. 6d,e).

300 4.3 Composite hailstorm life cycle

Moreover, in order to disentangle the different developmental stages of the storms, the storm-centered parameters were analyzed temporarily at the stages classified as *initiation*, *mature*, and *dissipation*. To this end, storms can be "synchronized" to their respective developmental stages and directly composited, even if the storms have different lifespans and evolutionary timing. The specific timing of the developmental stages is defined as follows:

305   – *initiation/start* — time when the storm is first detected by the tracking algorithm (more than 5 grid-points exceed $5\,\mathrm{m\,s^{-1}}$ updraft velocity).

    – *mature* — moment of strongest vertical wind velocity within the storm mask.

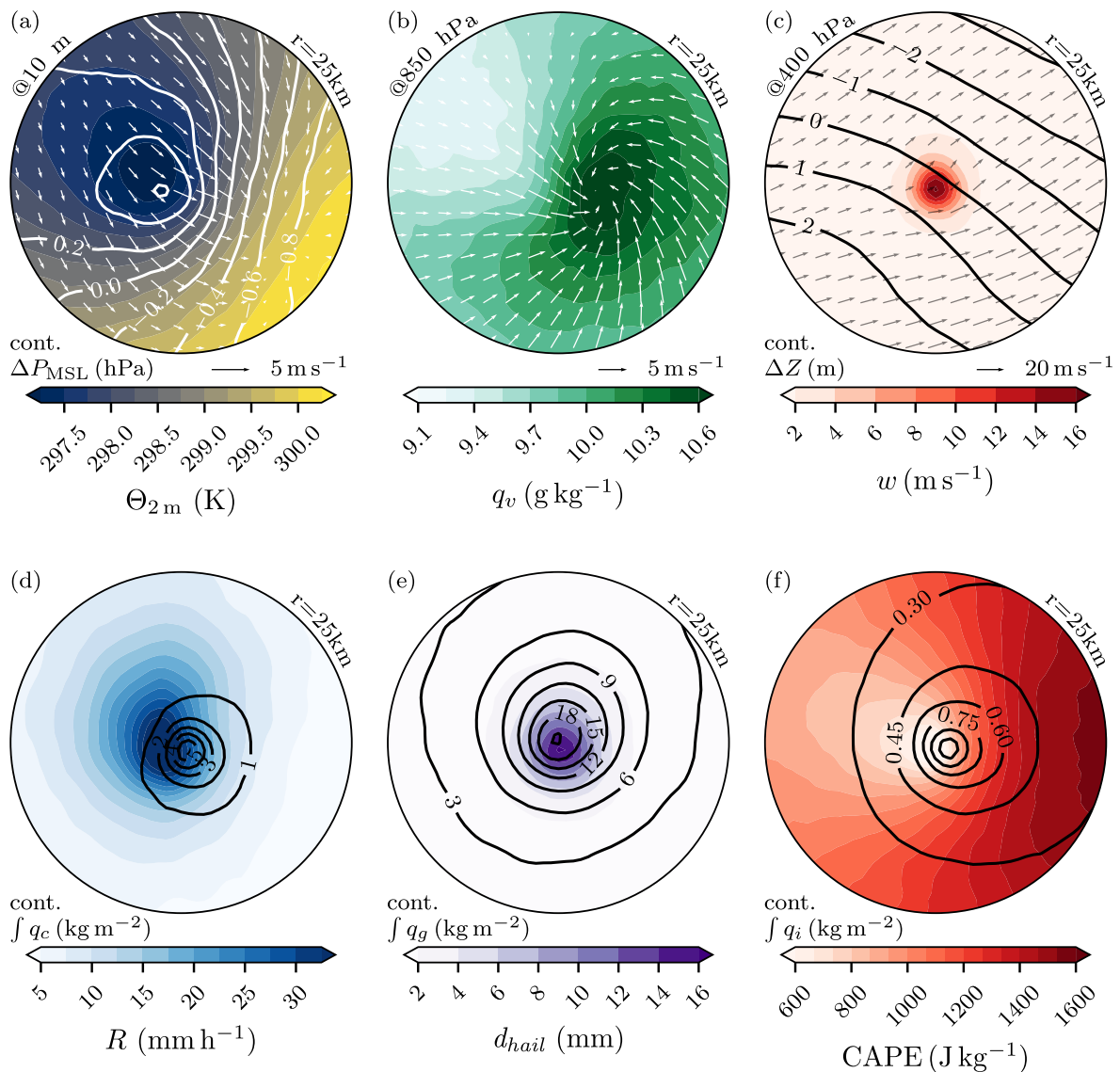   – *dissipation/end* — time when the storm is last detected by the tracking algorithm.

Figure 6. Composite analysis of the same $n = 100$ storms as shown in Fig. 5, centered on their track center and rotated so that their respective movement vectors align with the x axis (with the storm moving to the right). The radius of the figure outline is 25 km. (**a**) Near-ground conditions: White contours show the sea-level pressure anomaly relative to the mean across the composite, and the filled contours denote potential temperature at 2 m. White arrows show the 10 m wind field. (**b**) Inflow level: Specific humidity (filled contours) and horizontal wind field (quivers) at 850 hPa. (**c**) Updraft core level: geopotential height deviation from environment mean (black contours) and horizontal wind field (quivers) at 400 hPa. (**d**) Hourly rain rate (filled contours) and column-integrated cloud water (black contours). (**e**) HAILCAST maximum hail diameter (filled contours) and column integrated graupel (black contours). (**f**) CAPE (filled contours) and column integrated cloud ice (black contours).

From this, an intuitive progression of the vertical wind arises (Fig. 7b). Prior to storm initiation, vertical wind maxima
increase to $20 \, \mathrm{m \, s^{-1}}$. Just after initiation, the vertical wind stagnates. As storms reach their mature phase, the vertical wind
reaches a maximum, before reaching lower values again. Vertical winds exceed the baseline intensity for $\approx 1 \, \mathrm{h}$. Finally, the
reduced updraft intensity only becomes evident less than $0.5 \, \mathrm{h}$ before dissipation. The hail diameter generally follows the
evolution of vertical wind closely, while exhibiting a delay during the initiation and a less pronounced, broader maxima during
the mature phase (Fig. 7a). CAPE decreases steadily during all developmental phases while reaching its minimum during the
dissipation (Fig. 7c). There is no increase in environmental CAPE, as the storm reaches its mature phase. The storm area
follows the same general shape as the updraft, although it exhibits a minor delay of $15 \, \mathrm{min}$ during the mature phase (Fig. 7e).
Inflow air initially flows over higher terrain during the initiation phase and passes over lower terrain as it feeds the dissipating
storm (Fig. 7d). Contrary to the sequence of topographical height and storm vigor seen in 4, no such evidence was found
when investigating all storms in this regard. During the dissipation phase, starting $\approx 0.5 \, \mathrm{h}$ prior to the storm's end of life, the
mean inflow altitude markedly separates from the topography, while the inflow is on average around $600 \, \mathrm{m \, AGL}$ during the
storm's lifetime, and this changes to $800 \, \mathrm{m \, AGL}$ just before dissipation (not shown). Throughout the storm's lifetime, the bulk
of the inflow originates from 330–$900 \, \mathrm{m \, AGL}$, which is higher up than the 200–$400 \, \mathrm{m \, AGL}$ found in idealized simulations of
supercells (Coffer et al., 2023). The number of inflow trajectories filtered for ascent strongly increases up to a maximum just
before the storms reach their mature phase (Fig. 7f; see later section 5).

4.4 Storm-environmental parameters

Finally, a comprehensive view of the joint distribution of storm-environmental parameters is facilitated by investigating values
within a 50×50 grid-point box centered on the storm track for the same selection of storms as in Sect. 4.3. It allows us to
analyze the relationships and correlations between different variables. One notable correlation is between the hail diameter
(d_{hail}) and the vertical wind velocity (w), with a correlation coefficient of 0.776 (Fig. 8a). This strong positive correlation
suggests that larger hail diameters are associated with higher vertical wind velocities. In our analysis, CAPE does not correlate
with hail diameter, nor with w (Fig. 8b). On thermodynamic grounds, w would be expected to scale with $\sqrt{\mathrm{CAPE}}$. However,
the vertically integrated graupel shows a weak correlation coefficient with the hail diameter of 0.464 (Fig. 8c). One approach of
estimating hail is from the integrated graupel and in our case this approach would not explain the whole range of hail diameters
reported by HAILCAST. Larger hail diameters are also found at time steps when the vertical vorticity of the storm was highest
($c = 0.509$, Fig. 8d). Generally, large footprints are also associated with larger maximum hail diameters, however large hail
diameters can also be found in storms with smaller footprints ($c = 0.394$, Fig. 8e). Finally, it is important to note that this
analysis only provides a statistical view of the storm environment. To obtain a more physically meaningful perspective of the
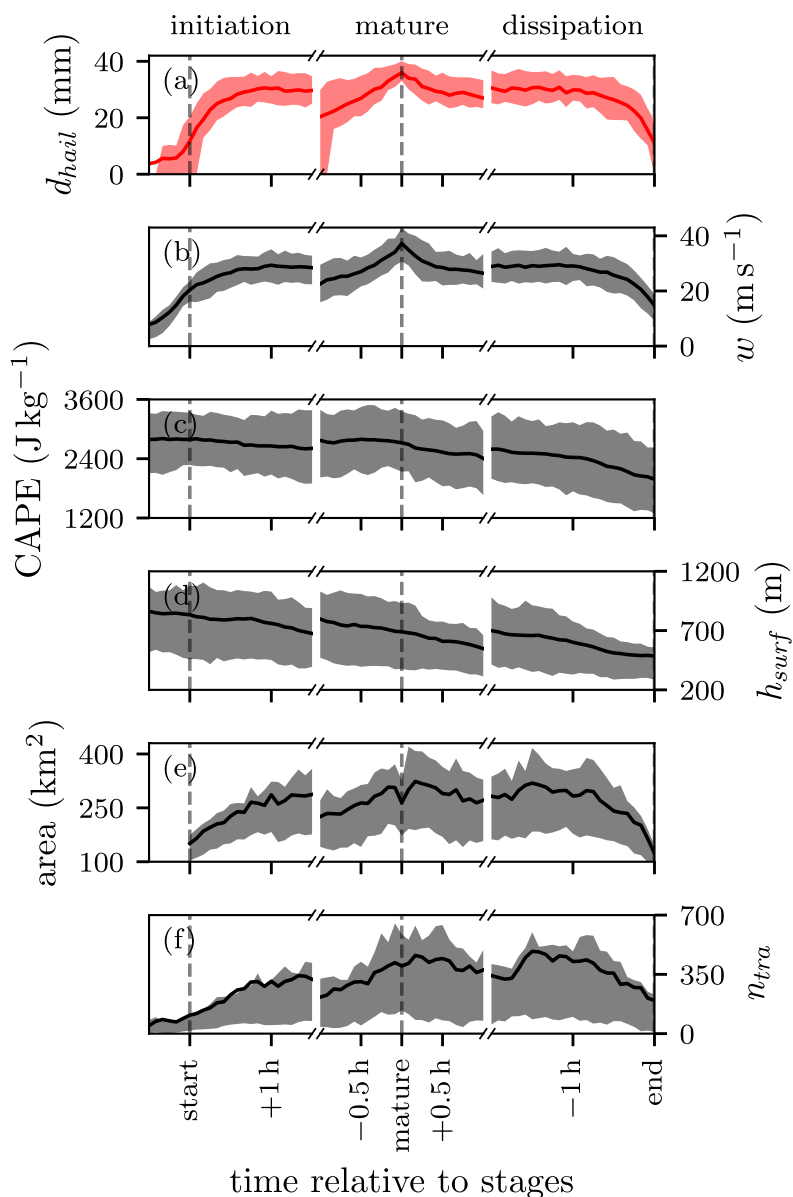air feeding the storm, we turn to Lagrangian inflow trajectories, which will be discussed in the following section.

Figure 7. Values for select variables within a 50×50 grid-point box centered on the storm position during three developmental stages of storms identified in all COSMO-1E members with lifespans $> 2.5\,\mathrm{h}$ that reach updraft velocities $> 25\,\mathrm{m\,s^{-1}}$. Shown are (**a**) maximum hail diameter d_{hail}, (**b**) vertical wind maximum, (**c**) maximum CAPE, (**d**) mean surface elevation, (**e**) storm area, and (**f**) number of trajectories. w and d_{hail} are masked by the storm track mask. The solid line represents the mean value across all storms, while the shaded area shows the interquartile range.
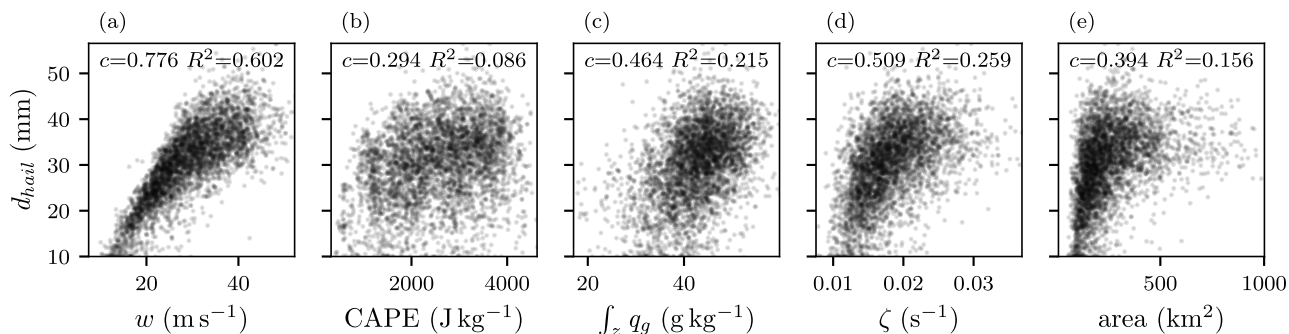
Figure 8. Scatter matrix with per time step storm-environmental parameters (considered in box with $50{\times}50$ gridpoints) from storms with lifespans $> 2.5\,\mathrm{h}$ that reach updraft velocities $> 25\,\mathrm{m\,s^{-1}}$. All values but the area are the per-time step maxima found within the environmental box. Correlation and R^2 values are indicated in each permutation. COSMO-1E simulation, all 11 members.

5 Lagrangian inflow trajectories

In this section, we discuss the Lagrangian perspective of the air parcels processed by the storm. Lagrangian trajectories were calculated using LAGRANTO (Wernli and Davies, 1997; Sprenger and Wernli, 2015) and 5-min wind fields from COSMO-1E. At each time step when a storm was active, points within the storm mask, laying on a $275 \times 275\,\mathrm{m}$ horizontal grid, at $z = 5000\,\mathrm{m}$ were selected as trajectory starting points. $2\,\mathrm{h}$ backwards as well as forwards trajectories were calculated with LAGRANTO using a $1\,\mathrm{min}$ time step, while the trace variables were recorded every $5\,\mathrm{min}$, consistent with the available model output time step. The resulting trajectories were filtered for ascent with the criterion of ascending at least $600\,\mathrm{hPa}$ within the $2\,\mathrm{h}$ centered on the time of storm intercept (when the trajectories traverse the $5000\,\mathrm{m}$ level), similar to filtering criteria used in warm conveyor belt studies (i.e. Heitmann et al., 2024).

To highlight the path of the inflow, we consider the trajectories arriving in the selected storm's updraft (as explained in Sect. 3.2) at the time of highest intensity. While the storm is propagating in a north-easterly direction, the bulk of the inflow is moving in the opposite direction. While the main inflow is initially broad and parallel, it narrows down and converges as it approaches the storm all while remaining close to the ground until arrival at the updraft (Fig. 9). Surprisingly, some stray parcels are also advected across the main Alpine crest before entering the updraft while still rising more than $600\,\mathrm{hPa}$ within the storm. Further, a broadening of the inflow sector can be observed at later times. While the inflow trajectories are almost parallel at 14:05, they markedly broaden as the storm passes maturity and approaches its dissipation.

Next, we consider various microphysical and thermodynamic properties of the air being processed by the storms (Fig. 10). The majority of the ascent of air parcels in the storm updraft is very rapid. The parcels are lofted from near-ground level to the tropopause in mere tens of minutes. During the inflow period, up to $-0.5\,\mathrm{h}$, the CAPE at the parcel height increases steadily, while the CIN is reduced until the storm is reached. During the ascent, CAPE is rapidly consumed, and latent heat is
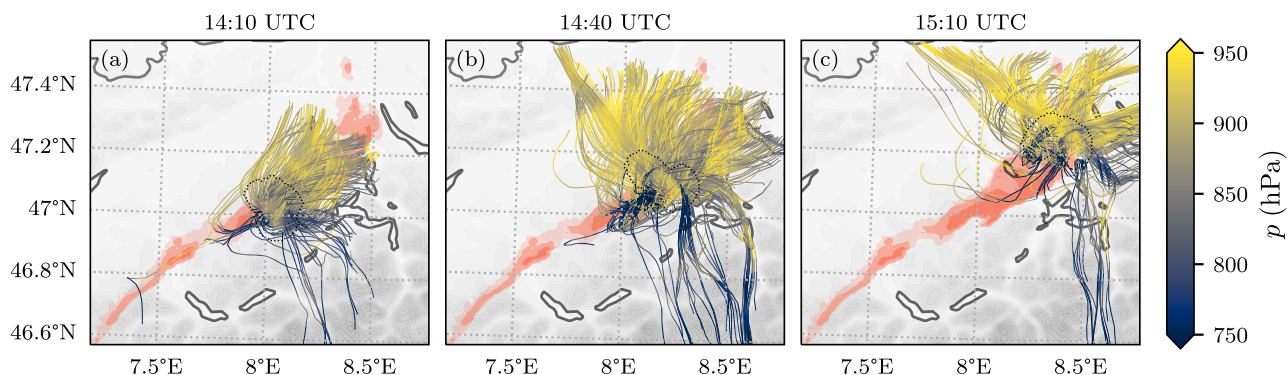
Figure 9. 2 h backward trajectories that are feeding a hailstorm updraft on 28 June 2021 during its most intense phase at 14:35 UTC (**b**) and 30 min prior and after the most intense phase (**a** & **c** respectively). Only trajectories that experience a change in pressure of $> 600\,\mathrm{hPa}$ are shown. The trajectories are colored with their local respective pressure. The red-filled contours show the maximum updraft swath areas that exceed velocities of 10, 20, and $30\,\mathrm{m\,s^{-1}}$ respectively, while the black dotted contour encloses the current storm mask. The gray shading represents topography height, while grey lines denote the national borders and lakes. COSMO-1E simulation.

released. The spread in parcel pressure during the inflow phase is very small, while there is a larger spread in the outflow phase (Fig. 10a).

To disentangle interactions between the different precipitation species and their effect on the inflow parcels, changes in Θ_e are investigated. The evolution of Θ_e during the inflow phase closely follows that of CAPE. After intercept, Θ_e returns to the same values as were present during the inflow phase. The parcels exclusively approach saturation during the intercept period, while moistening starts to occur at $t = -1\,\mathrm{h}$ relative to intercept (Fig. 10b). The development of the different microphysical species along the trajectories is as follows: The first species to increase in concentration is rain, followed by cloud, graupel, ice, and finally snow (Fig. 10c). Although some of the intercept-relative variables are more easily explained, such as the values in Fig. 10a, others have less trivial explanations. Θ_e is conserved through adiabatic processes, as well as during condensation of the parcel moisture. In the absence of moist convection, near-surface Θ_e is expected to increase during the day, due to surface radiative processes and surface moisture sources. This effect can be observed far upstream of the storm (Fig. 10b, -2 to $-1\,\mathrm{h}$). As latent heat is released in the updraft, Θ_e is expected to remain constant. However, a clear decrease in Θ_e with a minima at the time of intercept was found (Fig. 10b). Several, Θ_e-nonconserving phenomena offer explanations for the decrease and increase seen in Θ_e during inflow and outflow phases, respectively. Sensible heat flux from the rain entering the air parcel from above would reduce Θ_e, as the rainwater is colder than the air it enters and thus extracts heat energy from the parcel. As the air parcel is sub-saturated during the inflow period, there is also evaporative cooling from the infalling rain, however, this would not affect Θ_e, as the moistening of the parcel cancels it out. Most of the inflow occurs in the warm phase, however with the melting level at $\approx 650\,\mathrm{hPa}$ there are also some mixed-phase processes to consider. Graupel falling into the inflow parcel would also reduce Θ_e of the parcel, through the same effect discussed for the rainfall, with added cooling through the latent

18

heat needed to melt the solid phase. After the storm intercept in the mixed-phase cloud, the liquid species freeze to cloud ice, snow, and graupel, releasing latent heat, and thus increasing Θ_e. Vapour deposition of the gaseous phase to the ice phases is

380   also expected to increase Θ_e.

Another curious observation is that rain precedes the presence of cloud water in the inflow parcels (Fig. 10c). This rain can not be produced by the parcel itself, as the rain is present in sub-saturated conditions, and at times when no cloud water is present. As such, it must be rain that is falling into the updraft parcels from higher levels. Other studies have found fewer interactions of hydrometeors with the inflowing air (i.e. Coffer et al., 2023). These findings provide detailed insights into the

385   dynamic and thermodynamic processes affecting the inflow trajectories and their microphysical changes. They form the basis for the summary and conclusions in the next section.

6   Summary and conclusions

This study presents a detailed Lagrangian and Eulerian analysis of severe hailstorms that occurred in Switzerland on 28 June 2021 using the high-resolution convection-permitting ensemble hindcast COSMO-1E. Our comprehensive approach combines

390   object-based tracking techniques for hailstorms, Eulerian analysis of storm-associated atmospheric variables, and Lagrangian trajectory analysis of air parcels feeding into a hailstorm's updraft. Through a novel implementation of object-based tracking, we established the storm characteristics and compared them with recorded radar observations validating the simulated storm track against reality. We then systematically analyzed storms with a lifespan greater than $2.5\,\mathrm{h}$ and updraft velocities exceeding $25\,\mathrm{m\,s^{-1}}$, which revealed several long-lived and intense hailstorms within the simulation domain, mainly concentrated to the

395   north of the Alpine crest. COSMO-1E with HAILCAST simulates, for this case, realistic hail tracks in terms of storm lifetimes, storm area, propagation velocity and direction (Fig. 2,3).

The Eulerian perspective, focusing on atmospheric parameters and fields around the storms, allowed us to decompose the life cycle of hailstorms into initiation, mature, and dissipative stages. We investigated the temporal and spatial structure of the storm's composite creating an idealized picture of a hailstorm's profile, highlighting impressive updraft velocities, overshooting

400   tops, and the intricate cloud structures associated with severe hailstorms (Fig. 5). Archetypal hailstorm structures as simulated by COSMO confirm that rain-after-hail was prevalent for the storms occurring on this day (Fig. 6).

Lagrangian trajectory analysis provided physical insights into the inflow dynamics and source regions of air masses ingested by the hailstorm. We confirmed that most inflow air was channeled near the surface and could trace air parcel evolution, including CAPE and CIN consumption, saturation level, as well as progression of various hydrometeor species from unfrozen to

405   frozen states. The presence of rain prior to parcel saturation or cloud water and the changes in equivalent potential temperature suggest complex interactions between the precipitation species falling into the storm's updraft, thus transporting heat energy vertically. The analysis of airflow into hailstorms and investigation of Lagrangian evolution of CAPE, CIN and hydrometeors leads to the following conclusions: (i) rapid decrease of CAPE and CIN from $1100\,\mathrm{J/kg}$ and $-60\,\mathrm{J/kg}$ when air parcels converge into the updraft region; (ii) hydrometeor sequence shows rain predates all other microphysical species in the inflow

410   air parcels; (iii) origin of hailstorm air from various regions, notably air being drawn into storms and feeding the updraft from
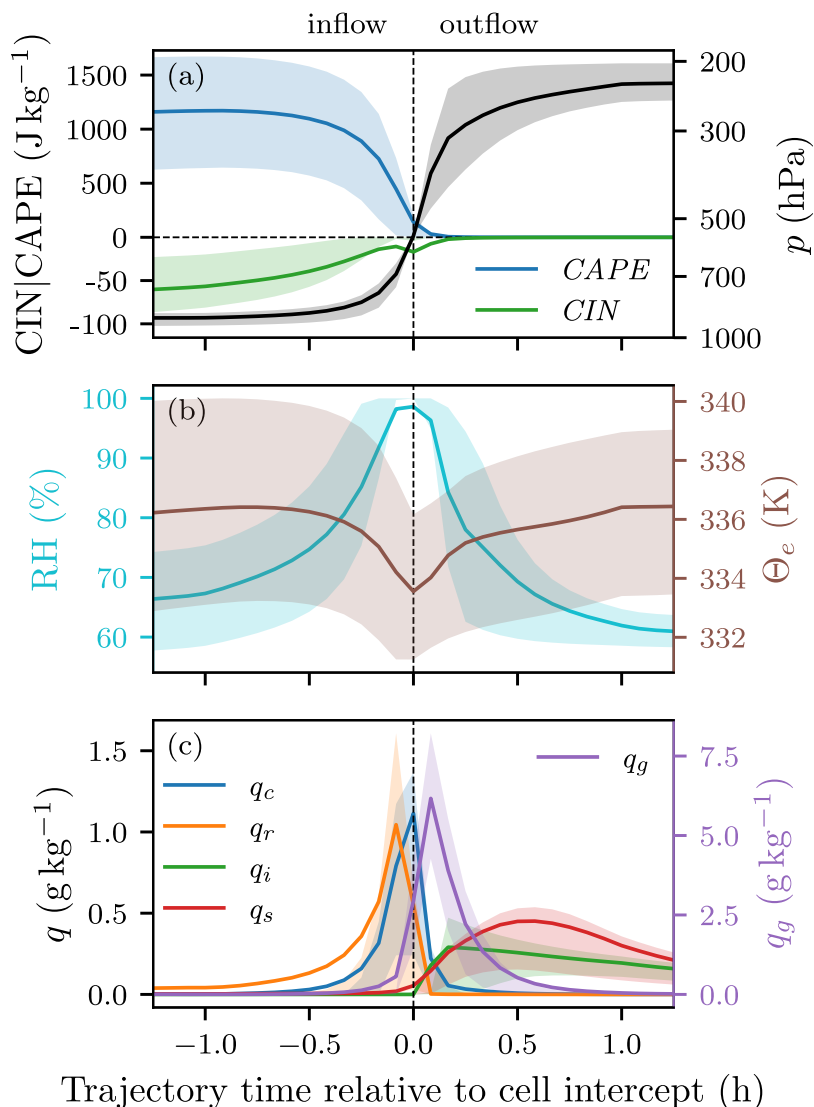
Figure 10. Various trace variables from all time steps of storms with lifespans $> 2.5\,\mathrm{h}$ that reach updraft velocities $> 25\,\mathrm{m\,s^{-1}}$ as a function of trajectory time relative to intercept of the trajectory with the storm at $z = 5000\,\mathrm{m}$. The solid lines show the mean for all trajectories of all storms and time steps at a given trajectory time, while the shaded areas indicate the interquartile range. The dotted line represents the storm intercept time. (**a**) CAPE & CIN at parcel height on the left axis and parcel pressure on the right axis. Note that CIN is on a different scale than CAPE. (**b**) Relative humidity and Θ_e of the parcel. (**c**) Microphysical species (cloud, rain, ice, snow and graupel) with q_g on the right axis, with different scaling. COSMO-1E simulation, all 11 members.

across the Alpine crest (Fig. 7, 10, 9). This study highlights the strength of combined Lagrangian and Eulerian analysis methods in furthering our understanding of the complex processes governing hailstorm evolution. The demonstrated object-based and

Lagrangian approach is a substantial step forward in severe storm studies, offering deeper insights than typically provided by Eulerian analysis alone.

415 The storm-centered perspective proved useful in analyzing the storm's structure and evolution, while the Lagrangian inflow trajectories provided insights into the air masses feeding the storm. The storm-centered composites could also prove to be useful in analyzing the changes in storm structure from convection-resolving climate simulations, whereas the available output frequency and vertical resolution available from climate simulations would likely not suffice for the Lagrangian analysis. The Lagrangian methodology could also be employed to diagnose the moisture sources of the hailstorms, or investigate the evolution 420 of vorticity in the air processed by the storm, and how this influences the rotation of the storm core. In conclusion, the ensemble simulation-based perspective leveraged in this study enhances our ability to explore hailstorm initiation, intensification, and dissipation mechanisms. It underscores the importance of considering both storm-scale dynamics and mesoscale environmental conditions in predicting and interpreting hailstorms. This research framework can be adapted and extended to other severe weather phenomena, thereby helping in developing better adaptive strategies for managing and mitigating the risks associated 425 with such events.

We would like to close this study by briefly reflecting on the more general implications of this model-based study for hail research, and its main limitations. For many decades, research on the dynamics of hailstorms was mainly driven by radar meteorology – for mainly three reasons: (i) radar data provide the most complete and detailed picture of the three-dimensional structure of hailstorms and their temporal evolution, (ii) the formation of hail is complicated and not routinely 430 implemented in operational weather prediction models, and (iii) kilometer-scale resolution (at least) and the explicit treatment of deep convection is required to realistically simulate the evolution of thunderstorms associated with hail. The advent of high-resolution weather prediction ensembles with a hail diagnostic enable detailed studies of hailstorm formation, their evolution, and in particular their interaction with the environment. As shown in this study, this approach can lead to interesting findings, for instance about the inflow into storm updrafts and the temporal evolution of CAPE along storm tracks, which would not 435 be available from other approaches. Clearly, such a novel approach also comes with limitations. At the moment, it appears to be very difficult to validate some of our findings with observations. Also, some results presented in this study might be very specific to the case investigated (i.e., not representative for hailstorms in Switzerland in general) and they might be model dependent. We therefore suggest that similar investigations will be done for other cases and other models, in particular also with modeling systems where hail is not diagnosed in the vertical column but explicitly simulated by the microphysics 440 parameterization.

Appendix A: Tracking algorithm

In this section, we describe the tracking algorithm `cell_tracker` in detail. The full Python code for the tracking algorithm is available at https://git.iac.ethz.ch/scclim/cell_tracker. Some of the parameters and thresholds chosen for this study were described in Sect. 2.2 and other default thresholds will be given throughout the following description, wherever a new algorithm parameter is introduced. The tracking algorithm was designed to be variable agnostic, and should, after tuning the thresholds and parameters, work with any two-dimensional field. To keep this description as universal as possible, wherever a threshold or parameter refers to the specific intensity value of the input field, we use intensity units (`iu`). The tracking functionality is provided by the function `track_cells` in the repository.

A1   Identification and segmentation

First, features are identified in a two-dimensional field using thresholds for various parameters described below. A feature constitutes a set of grid-points (`gp`) and has certain properties such as size, center of mass, magnitude, etc. Local maxima M are then defined as connected sets (4-connectivity) of grid-points with magnitudes strictly greater than the magnitudes of all pixels in the direct neighborhood of the set. Local maxima must fulfill the minimum distance threshold `min_distance = 6` and will be neglected otherwise. The `prominence` of a local maxima M is defined as the magnitude difference between M and the lowest isopleth encircling only M and local maxima with magnitudes smaller than M. Local maxima must satisfy the minimum prominence threshold of `prominence = 10iu` and will be neglected otherwise (function `label_local_maximas`). From a synthetic input field (Fig. A1a) with 6 objects in total, the segmentation algorithm classifies and labels 3 objects that fulfill the default tracking parameters (Fig. A1b). As visualized in Fig. A1c, initial object 1 does not fulfill the `threshold` criteria, while objects 2 through 6 exceed the `threshold`. Objects 2 through 4 are encircled by a contour greater than `threshold`, but object 4 is segmented due to sufficient `prominence`, objects 2 and 3 do not fulfill this criterion. Object 5 is segmented by the simple `threshold` criterion, while object 6 is discarded as it does not satisfy the `area` filter. Using local maxima obtained through the previous steps as seeds, a watershed segmentation algorithm is applied (Najman and Schmitt, 1994; van der Walt et al., 2014). The watershed algorithm treats magnitudes as topography (elevation) and floods basins from the seeds until basins attributed to different seeds meet on watershed lines (Fig. A1, objects 2,3 and 4). These basins are then associated with a unique label whose area encompasses a feature. The basins extend from M until the intensity exceeds the threshold `threshold = 5iu` (function `watershed`). In order to extend the label area spatially and increase tracking robustness, a binary dilation is applied through kernel convolution, which expands the label area into background regions by `aura = 3gp` while avoiding overlaps with neighboring label areas (function `expand_labels`. The resulting feature area must be larger than `min_area = 16gp`.

A1   Forward movement anticipation

Using a geometrically decaying weighted mean of the feature movement vector history of the last `dynamic_tracking = 4` time steps, the labeled area from the previous time step is shifted towards the expected position of the feature in the current
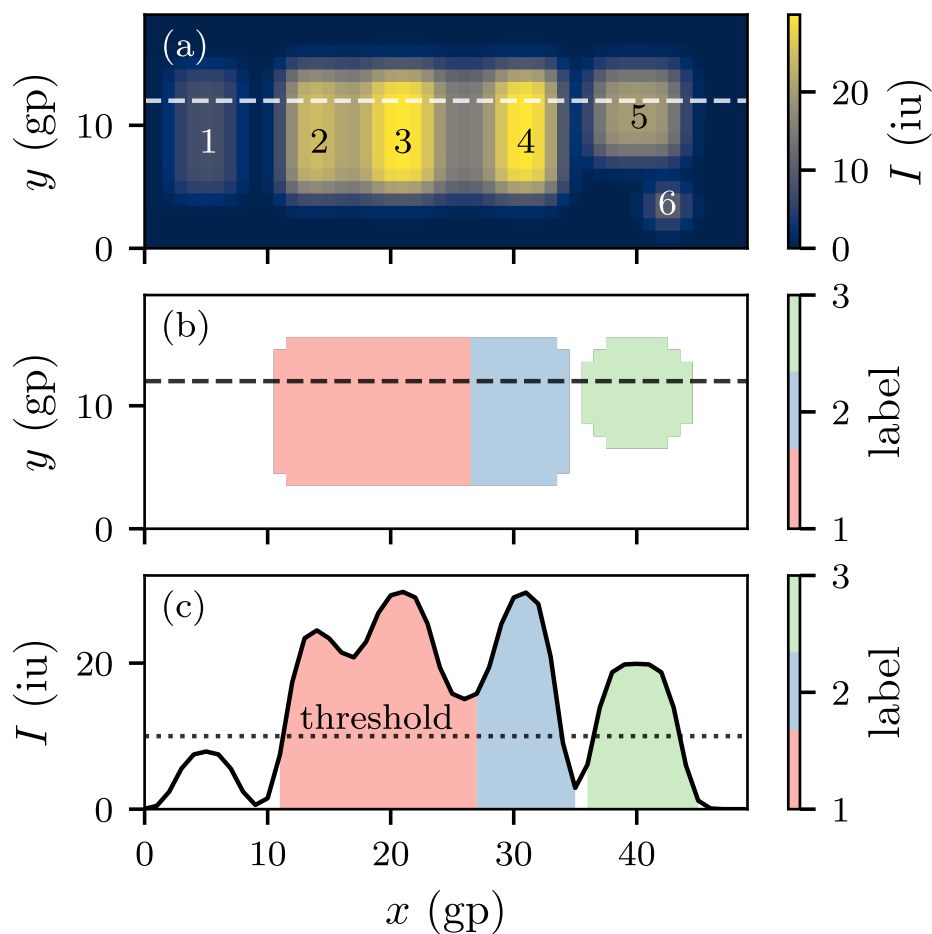
Figure A1. (**a**) Synthetic intensity field featuring 6 objects with varying intensities and areas. Dashed line indicates the position of the cross-section in panel **c**. (**b**) Object labels extracted from intensity field in panel b. Dashed line indicates the position of the cross-section in panel **c**. (**c**) Intensity along the cross-section indicated in panels a & b with the labeled objects indicated in color.

time step and is used as a search mask (function `advect_array`). If the feature first emerges and has no previous vector, a flow field is extracted from nearby features and used as an initial movement vector (function `generate_flow_field`). A limit is imposed on the maximum value for the advection of the search mask (`v_limit = 10gp`) to avoid erratic behavior and unphysical representation in the tracks of the atmospheric objects (e.g., track skipping along squall line).

A2 Correspondence algorithm

Finding corresponding features between the current and previous time steps is implemented by computing a tracking probability score for all correspondence candidates. First, for any given feature, active in the last time step, correspondence

candidates in the current time step are determined based on the nonzero overlap criterion from the advected search mask
(function `find_correspondences`). Next, all correspondence candidates are clustered into groups whose correspondence
assignment can be solved independently (function `find_cluster_members`). If multiple corresponding features are found
within an independent cluster, all possible candidate combination permutations are analyzed holistically for their overall track-
ing probability score within that cluster (function `correspond_cluster`). A weighted combination of the overlap surface
area ratio and the feature size ratio is taken into account to calculate the tracking score (function `calculate_score`). By
default, the overlap and surface area ratio are equally weighted (`alpha = 0.5`) to construct the score. A similar solution to
the correspondence problem was implemented by Rüdisühli (2018) and the probability score was directly adapted. Choosing
the most likely correspondence combination with the highest probability score leads to the attribution of features that either
start existing, carry on, cease to exist, split into multiple features, or are merged into another feature. The storm exhibiting the
largest area keeps the ID (parent), while the other is assigned to a new ID (child), while retaining the parent-child relationship.
During merging events, the more long-lived feature retains its ID, while the other merge participant ceases to exist, but while
retaining the merge relationship to the merge target.

Clusters with up to `cluster_size_limit = 16` correspondence possibilities leading to a permutation of size 2^{16}
can be scored efficiently (in $< 1\,\mathrm{s}$, single core, Intel® Xeon® CPU E5-2690 v4 @ 2.60GHz). If the cluster size exceeds
`cluster_size_limit`, the candidates with the smallest overlap are pruned if they can be assigned to other features,
so only the 16 candidates with the largest overlap area are considered for the correspondence (function `prune_cluster`).
Exceptions where cluster pruning is not sufficient to reduce the cluster size, further reduction in cluster size is handled by
`crude_correspondence`. The crude assignment starts by assigning the object with the smallest area to the candidate with
the best score until the `cluster_size_limit` is respected. Note that for the crudely assigned correspondences only contin-
ued survival and no splitting/merging is possible. This significantly improves tracking performance for large clusters. However,
it should be mentioned here that reaching large cluster sizes can hint towards non-optimal choices for tracking parameters and
fine-tuning thereof should be strongly considered, rather than relying on cluster-pruning and crude correspondence.

A3 Swath gap filling

One application of the storm tracks includes reducing the 'fishbone effect', a term coined in Lukach et al. (2017), describing
the discontinuous hail swaths caused by the low temporal sampling of fast-moving and short (in the direction of movement)
storms. The 'fishbone effect' could especially bias damage models, as the hail-affected area is underestimated, especially for
large hail diameters. Gaps in the hail swaths are present, even with a relatively high temporal sampling of $5\,\mathrm{min}$ (Fig. B1a).

To fill the hail swath gaps (function `fill_gaps`), storm footprints from two adjacent time steps can be linearly interpolated
to form an intermittent storm footprint at a virtual time step μ. The intermittent storm footprints are then translated to their
linearly interpolated positions determined from the storm movement vector $\boldsymbol{v}$ and compounded using:

$$\Psi^n = \max\left(\left[\frac{\mu}{\kappa}\psi^n_{i+\boldsymbol{v}\frac{\mu}{\kappa}} + \left(1-\frac{\mu}{\kappa}\right)\psi^{n+1}_{i-\boldsymbol{v}\left(1-\frac{\mu}{\kappa}\right)}\right]_{\mu\in\{\mathbb{N}\leq\kappa\}}\right), \tag{A1}$$

where Ψ^n is the linearly interpolated swath at time step n, ψ_i^n is the storm footprint at time n and position i as determined by the tracking algorithm, $\kappa = {}_{\Delta}t_{virt.}/{}_{\Delta}t$ is the number of virtual time steps per simulation output time step. Translations are performed at the grid-point level, and the derivations of v are rounded to the nearest integer, ignoring sub-grid-point translations. Ψ can be calculated for all time steps in which the storm is active, yielding the total smoothed swath area $\mathbb{S}$:

$$\mathbb{S} = \max\left([\Psi^n]_{n \in \gamma}\right), \tag{A2}$$

where γ contains all time steps where the storm is active. The described implementation bridges the gaps left by the sparse temporal sampling of the fast-moving, small hailstorms, while conserving small-scale details, even in the presence of complex features, like crossing tracks, bowed squall lines, and multiple maxima within storm extents (Fig. B1b). With gap filling ($\kappa = 5$), the swath areas ($> 20\,\mathrm{mm}$) are a factor two larger than the swaths reported using the original $5\,\mathrm{min}$ time step (Fig. B1c).

525 **Appendix C: Single storm cross-section**

530 *Competing interests.* At least one of the (co-)authors is a member of the editorial board of *Weather and Climate Dynamics*.

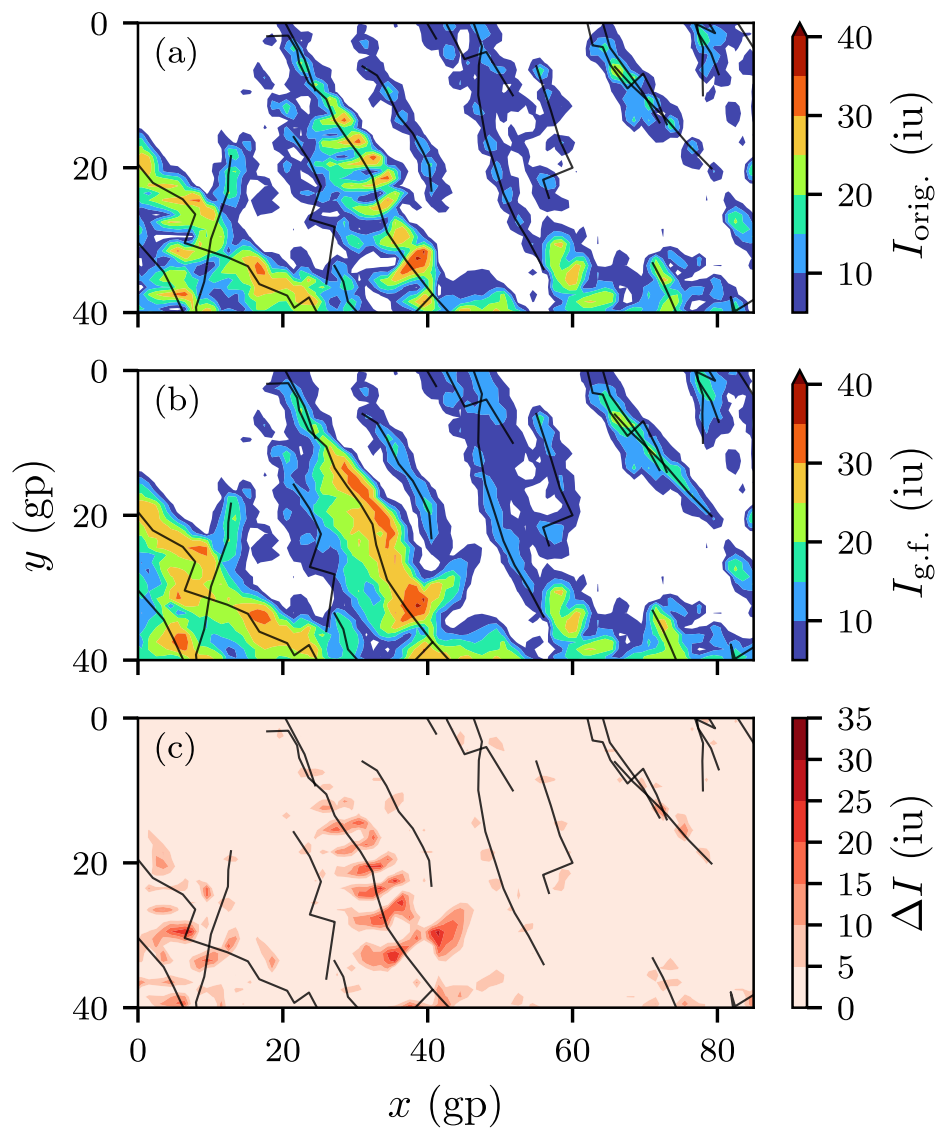**Figure B1.** (**a**) Time-maximum original intensity field visualized as filled contours with storm tracks overlaid as black lines. (**b**) Same as panel a but with gap filling enabled. (**c**) Intensity added by gap filling, or difference in intensity between panel a and b.

References

535 Adams-Selin, R. D. and Ziegler, C. L.: Forecasting Hail Using a One-Dimensional Hail Growth Model within WRF, Mon. Weather Rev., 144, 4919–4939, https://doi.org/10.1175/MWR-D-16-0027.1, 2016.
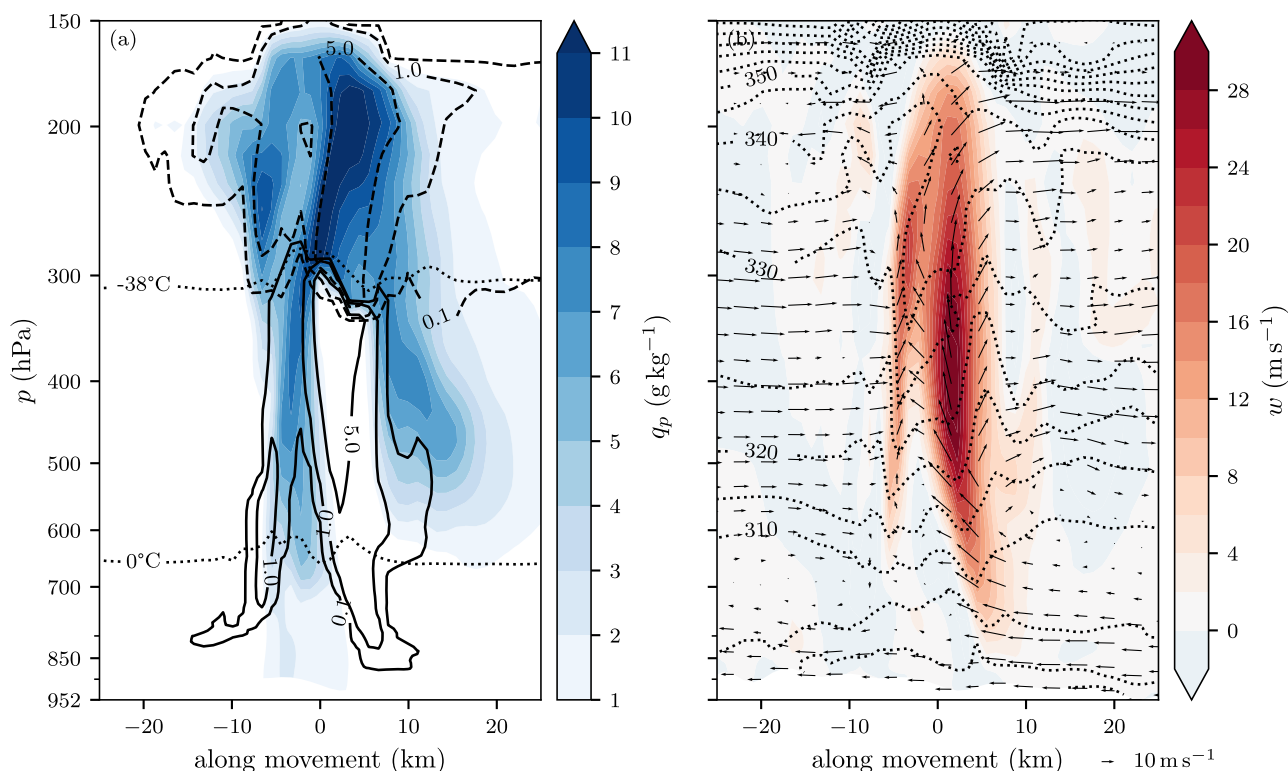
Figure D1. Same as Fig. 5, for the most intense time step of a selected storm.

Adams-Selin, R. D., Clark, A. J., Melick, C. J., Dembek, S. R., Jirak, I. L., and Ziegler, C. L.: Evolution of WRF-HAILCAST during the 2014–16 NOAA/Hazardous Weather Testbed Spring Forecasting Experiments, Weather Forecast., 34, 61–79, https://doi.org/10.1175/WAF-D-18-0024.1, 2019.

540 Allen, J. T., Giammanco, I. M., Kumjian, M. R., Jurgen Punge, H., Zhang, Q., Groenemeijer, P., Kunz, M., and Ortega, K.: Understanding Hail in the Earth System, Rev. Geophys., 58, https://doi.org/10.1029/2019RG000665, 2020.

BAFU: Umgang Mit Naturgefahren in Der Schweiz. Bericht Des Bundesrats in Erfüllung Des Postulats 12.4271 Darbellay Vom 14.12. 2012, 2016.

Baldauf, M., Seifert, A., Förstner, J., Majewski, D., Raschendorfer, M., and Reinhardt, T.: Operational Convective-Scale Numerical Weather
545 Prediction with the COSMO Model: Description and Sensitivities, Mon. Weather Rev., 139, 3887–3905, https://doi.org/10.1175/MWR-D-10-05013.1, 2011.

Barras, H., Martius, O., Nisi, L., Schroeer, K., Hering, A., and Germann, U.: Multi-Day Hail Clusters and Isolated Hail Days in Switzerland – Large-Scale Flow Conditions and Precursors, Weather Clim. Dynam., 2, 1167–1185, https://doi.org/10.5194/wcd-2-1167-2021, 2021.

Barthlott, C. and Barrett, A. I.: Large Impact of Tiny Model Domain Shifts for the Pentecost 2014 Mesoscale Convective System over
550 Germany, Weather Clim. Dynam., 1, 207–224, https://doi.org/10.5194/wcd-1-207-2020, 2020.

Barthlott, C. and Kalthoff, N.: A Numerical Sensitivity Study on the Impact of Soil Moisture on Convection-Related Parameters and Convective Precipitation over Complex Terrain, J. Atmos. Sci., 68, 2971–2987, https://doi.org/10.1175/JAS-D-11-027.1, 2011.

Bechis, H., Galligani, V., Alvarez Imaz, M., Cancelada, M., Simone, I., Piscitelli, F., Maldonado, P., Salio, P., and Nesbitt, S. W.: A Case Study of a Severe Hailstorm in Mendoza, Argentina, during the RELAMPAGO-CACTI Field Campaign, Atmos. Res., 271, 106 127, https://doi.org/10.1016/j.atmosres.2022.106127, 2022.

Bluestein, H. B.: Severe Convective Storms and Tornadoes: Observations and Dynamics, Springer, Berlin, Heidelberg, https://doi.org/10.1007/978-3-642-05381-8, 2013.

Brimelow, J.: Hail and Hailstorms, p. 58, Oxford University Press, https://doi.org/10.1093/acrefore/9780190228620.013.666, 2018.

Brimelow, J. C.: Numerical Modelling of Hailstone Growth in Alberta Storms, M.S. Thesis, University of Alberta, Dept. of Earth and Atmospheric Sciences, 1999.

Brimelow, J. C., Reuter, G. W., and Poolman, E. R.: Modeling Maximum Hail Size in Alberta Thunderstorms, Weather Forecast., 17, 1048–1062, https://doi.org/10.1175/1520-0434(2002)017<1048:MMHSIA>2.0.CO;2, 2002.

Calvo-Sancho, C., Díaz-Fernández, J., Martín, Y., Bolgiani, P., Sastre, M., González-Alemán, J. J., Santos-Muñoz, D., Farrán, J. I., and Martín, M. L.: Supercell Convective Environments in Spain Based on ERA5: Hail and Non-Hail Differences, Weather and Climate Dynamics, 3, 1021–1036, https://doi.org/10.5194/wcd-3-1021-2022, 2022.

Changnon, S. A.: Data and Approaches for Determining Hail Risk in the Contiguous United States, J. Appl. Meteorol. Clim., 38, 1730–1739, https://doi.org/10.1175/1520-0450(1999)038<1730:DAAFDH>2.0.CO;2, 1999.

Coffer, B. E., Parker, M. D., Peters, J. M., and Wade, A. R.: Supercell Low-Level Mesocyclones: Origins of Inflow and Vorticity, Mon. Weather Rev., 151, 2205–2232, https://doi.org/10.1175/MWR-D-22-0269.1, 2023.

Crompton, R. P. and McAneney, K. J.: Normalised Australian Insured Losses from Meteorological Hazards: 1967–2006, Environ. Sci. Policy, 11, 371–378, https://doi.org/10.1016/j.envsci.2008.01.005, 2008.

Ducrocq, V., Nuissier, O., Ricard, D., Lebeaupin, C., and Thouvenin, T.: A Numerical Study of Three Catastrophic Precipitating Events over Southern France. II: Mesoscale Triggering and Stationarity Factors, Q. J. Roy. Meteor. Soc., 134, 131–145, https://doi.org/10.1002/qj.199, 2008.

Feldmann, M., Germann, U., Gabella, M., and Berne, A.: A Characterisation of Alpine Mesocyclone Occurrence, Weather Clim. Dynam., 2, 1225–1244, https://doi.org/10.5194/wcd-2-1225-2021, 2021.

Gowan, T. M., Steenburgh, W. J., and Minder, J. R.: Downstream Evolution and Coastal-to-Inland Transition of Landfalling Lake-Effect Systems, Mon. Weather Rev., 149, 1023–1040, https://doi.org/10.1175/MWR-D-20-0253.1, 2021.

Graf, M., Sprenger, M., and Moore, R.: Central European Tornado Environments as Viewed from a Potential Vorticity and Lagrangian Perspective, Atmos. Res., 101, 31–45, https://doi.org/10.1016/j.atmosres.2011.01.007, 2011.

Gropp, M. E. and Davenport, C. E.: Python-Based Supercell Tracking for Coarse Temporal and Spatial Resolution Numerical Model Simulations, J. Atmos. Ocean. Tech., 38, 1551–1559, https://doi.org/10.1175/JTECH-D-20-0122.1, 2021.

Heitmann, K., Sprenger, M., Binder, H., Wernli, H., and Joos, H.: Warm Conveyor Belt Characteristics and Impacts along the Life Cycle of Extratropical Cyclones: Case Studies and Climatological Analysis Based on ERA5, Weather Clim. Dynam., 5, 537–557, https://doi.org/10.5194/wcd-5-537-2024, 2024.

Hering, A., Morel, C., Galli, G., Senesi, S., Ambrosetti, P., and Boscacci, M.: Nowcasting Thunderstorms in the Alpine Region Using a Radar Based Adaptive Thresholding Scheme, Proceedings of ERAD, 2004.

Hersbach, H., Bell, B., Berrisford, P., Hirahara, S., Horányi, A., Muñoz-Sabater, J., Nicolas, J., Peubey, C., Radu, R., Schepers, D., Simmons, A., Soci, C., Abdalla, S., Abellan, X., Balsamo, G., Bechtold, P., Biavati, G., Bidlot, J., Bonavita, M., De Chiara, G., Dahlgren, P., Dee, D., Diamantakis, M., Dragani, R., Flemming, J., Forbes, R., Fuentes, M., Geer, A., Haimberger, L., Healy, S., Hogan, R. J., Hólm, E., Janisková, M., Keeley, S., Laloyaux, P., Lopez, P., Lupu, C., Radnoti, G., de Rosnay, P., Rozum, I., Vamborg, F., Villaume, S., and Thépaut, J.-N.: The ERA5 Global Reanalysis, Q. J. Roy. Meteor. Soc., 146, 1999–2049, https://doi.org/10.1002/qj.3803, 2020.

Houze, R. A.: Cloud Dynamics, vol. 104, Elsevier, https://doi.org/10.1016/B978-0-12-374266-7.09992-3, 2014.

Houze, R. A., Schmid, W., Fovell, R. G., and Schiesser, H.-H.: Hailstorms in Switzerland: Left Movers, Right Movers, and False Hooks, Mon. Weather Rev., 121, 3345–3370, https://doi.org/10.1175/1520-0493(1993)121<3345:HISLMR>2.0.CO;2, 1993.

Jewell, R. and Brimelow, J.: Evaluation of Alberta Hail Growth Model Using Severe Hail Proximity Soundings from the United States, Weather Forecast., 24, 1592–1609, https://doi.org/10.1175/2009WAF2222230.1, 2009.

Klasa, C., Arpagaus, M., Walser, A., and Wernli, H.: An Evaluation of the Convection-Permitting Ensemble COSMO-E for Three Contrasting Precipitation Events in Switzerland, Q. J. Roy. Meteor. Soc., 144, 744–764, https://doi.org/10.1002/qj.3245, 2018.

Klasa, C., Arpagaus, M., Walser, A., and Wernli, H.: On the Time Evolution of Limited-Area Ensemble Variance: Case Studies with the Convection-Permitting Ensemble COSMO-E, J. Atmos. Sci., 76, 11–26, https://doi.org/10.1175/JAS-D-18-0013.1, 2019.

Kopp, J., Schröer, K., Schwierz, C., Hering, A., Germann, U., and Martius, O.: The Summer 2021 Switzerland Hailstorms: Weather Situation, Major Impacts and Unique Observational Data, Weather, https://doi.org/10.1002/wea.4306, 2022.

Lainer, M., Brennan, K. P., Hering, A., Kopp, J., Monhart, S., Wolfensberger, D., and Germann, U.: Drone-Based Photogrammetry Combined with Deep Learning to Estimate Hail Size Distributions and Melting of Hail on the Ground, Atmos. Meas. Tech., 17, 2539–2557, https://doi.org/10.5194/amt-17-2539-2024, 2024.

Lin, Y. and Kumjian, M. R.: Influences of CAPE on Hail Production in Simulated Supercell Storms, J. Atmos. Sci., 79, 179–204, https://doi.org/10.1175/JAS-D-21-0054.1, 2022.

Liu, Y., Qian, Y., Berg, L. K., Feng, Z., Li, J., Chen, J., and Yang, Z.: Tracking Precipitation Features and Associated Large-Scale Environments over Southeastern Texas, EGUsphere, pp. 1–24, https://doi.org/10.5194/egusphere-2024-112, 2024.

Lorenz, E. N.: Deterministic Nonperiodic Flow, J. Atmos. Sci., 20, 130–141, https://doi.org/10.1175/1520-0469(1963)020<0130:DNF>2.0.CO;2, 1963.

Lukach, M., Foresti, L., Giot, O., and Delobbe, L.: Estimating the Occurrence and Severity of Hail Based on 10 Years of Observations from Weather Radar in Belgium: Estimating Radar-Based Occurrence and Severity of Hail in Belgium, Meteorol. Appl., 24, 250–259, https://doi.org/10.1002/met.1623, 2017.

Marcos, J., Sánchez, J., Merino, A., Melcón, P., Mérida, G., and García-Ortega, E.: Spatial and Temporal Variability of Hail Falls and Estimation of Maximum Diameter from Meteorological Variables, Atmos. Res., 247, 105 142, https://doi.org/10.1016/j.atmosres.2020.105142, 2021.

Markowski, P. and Richardson, Y.: Mesoscale Meteorology in Midlatitudes, Wiley, 1 edn., https://doi.org/10.1002/9780470682104, 2010.

Meredith, E. P., Ulbrich, U., and Rust, H. W.: Cell Tracking of Convective Rainfall: Sensitivity of Climate-Change Signal to Tracking Algorithm and Cell Definition (Cell-TAO v1.0), Geosci. Model Dev., 16, 851–867, https://doi.org/10.5194/gmd-16-851-2023, 2023.

Mohr, S., Wilhelm, J., Wandel, J., Kunz, M., Portmann, R., Punge, H. J., Schmidberger, M., Quinting, J. F., and Grams, C. M.: The Role of Large-Scale Dynamics in an Exceptional Sequence of Severe Thunderstorms in Europe May–June 2018, Weather Clim. Dynam., 1, 325–348, https://doi.org/10.5194/wcd-1-325-2020, 2020.

625 Najman, L. and Schmitt, M.: Watershed of a Continuous Function, Signal Process., 38, 99–112, https://doi.org/10.1016/0165-1684(94)90059-0, 1994.

Neu, U., Akperov, M. G., Bellenbaum, N., Benestad, R., Blender, R., Caballero, R., Cocozza, A., Dacre, H. F., Feng, Y., Fraedrich, K., Grieger, J., Gulev, S., Hanley, J., Hewson, T., Inatsu, M., Keay, K., Kew, S. F., Kindem, I., Leckebusch, G. C., Liberato, M. L. R., Lionello, P., Mokhov, I. I., Pinto, J. G., Raible, C. C., Reale, M., Rudeva, I., Schuster, M., Simmonds, I., Sinclair, M., Sprenger, M., Tilinina, N. D.,
630 Trigo, I. F., Ulbrich, S., Ulbrich, U., Wang, X. L., and Wernli, H.: IMILAST: A Community Effort to Intercompare Extratropical Cyclone Detection and Tracking Algorithms, B. Am. Meteorol. Soc., 94, 529–547, 2013.

Nisi, L., Martius, O., Hering, A., Kunz, M., and Germann, U.: Spatial and Temporal Distribution of Hailstorms in the Alpine Region: A Long-Term, High Resolution, Radar-Based Analysis, Q. J. Roy. Meteor. Soc., 142, 1590–1604, https://doi.org/10.1002/qj.2771, 2016.

Noppel, H., Blahak, U., Seifert, A., and Beheng, K. D.: Simulations of a Hailstorm and the Impact of CCN Using an Advanced Two-Moment
635 Cloud Microphysical Scheme, Atmos. Res., 96, 286–301, https://doi.org/10.1016/j.atmosres.2009.09.008, 2010.

Palmer, T. and Hagedorn, R., eds.: Predictability of Weather and Climate, Cambridge University Press, Cambridge, https://doi.org/10.1017/CBO9780511617652, 2006.

Poolman, E. R.: Die Voorspelling van Haelkorrelgroei in Suid-Afrika (The Forecasting of Hail Growth in South Africa)., M.S. Thesis, Faculty of Engineering, University of Pretoria, Pretoria, 1992.

640 Portmann, R., Schmid, T., Villiger, L., Bresch, D. N., and Calanca, P.: Modelling Crop Hail Damage Footprints with Single-Polarization Radar: The Roles of Spatial Resolution, Hail Intensity, and Cropland Density, Preprint, Atmospheric, Meteorological and Climatological Hazards, https://doi.org/10.5194/egusphere-2023-2598, 2023.

Prein, A. F. and Heymsfield, A. J.: Increased Melting Level Height Impacts Surface Precipitation Phase and Intensity, Nat. Clim. Change, 10, 771–776, https://doi.org/10.1038/s41558-020-0825-x, 2020.

645 Pruppacher, H. R. and Klett, J. D.: Microphysics of Clouds and Precipitation, Atmospheric and Oceanographic Sciences Library, Springer Netherlands, 2 edn., 2010.

Purr, C., Brisson, E., and Ahrens, B.: Convective Shower Characteristics Simulated with the Convection-Permitting Climate Model COSMO-CLM, Atmosphere, 10, 810, https://doi.org/10.3390/atmos10120810, 2019.

Ridder, N. N., Pitman, A. J., Westra, S., Ukkola, A., Do, H. X., Bador, M., Hirsch, A. L., Evans, J. P., Di Luca, A., and Zscheischler, J.:
650 Global Hotspots for the Occurrence of Compound Events, Nat. Commun., 11, 5956, https://doi.org/10.1038/s41467-020-19639-3, 2020.

Rigo, T., Rodríguez, O., Bech, J., and Farnell, C.: An Observational Analysis of Two Companion Supercell Storms over Complex Terrain, Atmos. Res., 272, 106 149, https://doi.org/10.1016/j.atmosres.2022.106149, 2022.

Rüdisühli, S.: Attribution of Rain to Cyclones and Fronts over Europe in a Kilometer-Scale Regional Climate Simulation, Ph.D. thesis, ETH Zurich, https://doi.org/10.3929/ETHZ-B-000351234, 2018.

655 Rüdisühli, S., Sprenger, M., Leutwyler, D., Schär, C., and Wernli, H.: Attribution of Precipitation to Cyclones and Fronts over Europe in a Kilometer-Scale Regional Climate Simulation, Weather Clim. Dynam., 1, 675–699, https://doi.org/10.5194/wcd-1-675-2020, 2020.

Schär, C., Fuhrer, O., Arteaga, A., Ban, N., Charpilloz, C., Di Girolamo, S., Hentgen, L., Hoefler, T., Lapillonne, X., Leutwyler, D., Osterried, K., Panosetti, D., Rüdisühli, S., Schlemmer, L., Schulthess, T. C., Sprenger, M., Ubbiali, S., and Wernli, H.: Kilometer-Scale Climate Models: Prospects and Challenges, B. Am. Meteorol. Soc., 101, E567–E587, https://doi.org/10.1175/BAMS-D-18-0167.1, 2020.

660 Schemm, S., Rüdisühli, S., and Sprenger, M.: The Life Cycle of Upper-Level Troughs and Ridges: A Novel Detection Method, Climatologies and Lagrangian Characteristics, Weather Clim. Dynam., 1, 459–479, https://doi.org/10.5194/wcd-1-459-2020, 2020.

Schiesser, H. H., Houze, R. A., and Huntrieser, H.: The Mesoscale Structure of Severe Precipitation Systems in Switzerland, Mon. Weather Rev., 123, 2070–2097, https://doi.org/10.1175/1520-0493(1995)123<2070:TMSOSP>2.0.CO;2, 1995.

Schmid, T., Portmann, R., Villiger, L., Schröer, K., and Bresch, D. N.: An Open-Source Radar-Based Hail Damage Model for Buildings and Cars, Nat. Hazard Earth Sys., 24, 847–872, https://doi.org/10.5194/nhess-24-847-2024, 2024.

Schmid, W., Schiesser, H.-H., and Bauer-Messmer, B.: Supercell Storms in Switzerland: Case Studies and Implications for Nowcasting Severe Winds with Doppler Radar, Meteorol. Appl., 4, 49–67, https://doi.org/10.1017/S1350482797000388, 1997.

Seifert, A. and Beheng, K. D.: A Two-Moment Cloud Microphysics Parameterization for Mixed-Phase Clouds. Part 1: Model Description, Meteorol. Atmos. Phys., 92, 45–66, https://doi.org/10.1007/s00703-005-0112-4, 2006.

Sprenger, M. and Wernli, H.: The LAGRANTO Lagrangian Analysis Tool – Version 2.0, Geosci. Model Dev., 8, 2569–2586, https://doi.org/10.5194/gmd-8-2569-2015, 2015.

Steppeler, J., Doms, G., Schättler, U., Bitzer, H. W., Gassmann, A., Damrath, U., and Gregoric, G.: Meso-Gamma Scale Forecasts Using the Nonhydrostatic Model LM, Meteorol. Atmos. Phys., 82, 75–96, https://doi.org/10.1007/s00703-001-0592-9, 2003.

Sun, J., Xue, M., Wilson, J. W., Zawadzki, I., Ballard, S. P., Onvlee-Hooimeyer, J., Joe, P., Barker, D. M., Li, P.-W., Golding, B., Xu, M., and Pinto, J.: Use of NWP for Nowcasting Convective Precipitation: Recent Progress and Challenges, B. Am. Meteorol. Soc., 95, 409–426, https://doi.org/10.1175/BAMS-D-11-00263.1, 2014.

Taszarek, M., Brooks, H. E., and Czernecki, B.: Sounding-Derived Parameters Associated with Convective Hazards in Europe, Mon. Weather Rev., 145, 1511–1528, https://doi.org/10.1175/MWR-D-16-0384.1, 2017.

Taszarek, M., Allen, J. T., Púčik, T., Hoogewind, K. A., and Brooks, H. E.: Severe Convective Storms across Europe and the United States. Part II: ERA5 Environments Associated with Lightning, Large Hail, Severe Wind, and Tornadoes, J. Climate, 33, 10 263–10 286, https://doi.org/10.1175/JCLI-D-20-0346.1, 2020.

Trefalt, S., Martynov, A., Barras, H., Besic, N., Hering, A. M., Lenggenhager, S., Noti, P., Röthlisberger, M., Schemm, S., Germann, U., and Martius, O.: A Severe Hail Storm in Complex Topography in Switzerland - Observations and Processes, Atmos. Res., 209, 76–94, https://doi.org/10.1016/j.atmosres.2018.03.007, 2018.

Trefalt, S., Germann, U., Hering, A., Clementi, L., Boscacci, M., Schröer, K., and Schwierz, C.: Hail Climate Switzerland Operational Radar Hail Detection Algorithms at MeteoSwiss: Quality Assessment and Improvement, Technical Report 284, MeteoSwiss, 2023.

Ulbrich, C. W. and Atlas, D.: Hail Parameter Relations: A Comprehensive Digest, J. Appl. Meteor., 21, 22–43, 1982.

van der Walt, S., Schönberger, J. L., Nunez-Iglesias, J., Boulogne, F., Warner, J. D., Yager, N., Gouillart, E., and Yu, T.: Scikit-Image: Image Processing in Python, PeerJ, 2, e453, https://doi.org/10.7717/peerj.453, 2014.

Wernli, H. and Davies, H. C.: A Lagrangian-based Analysis of Extratropical Cyclones. I: The Method and Some Applications, Q. J. Roy. Meteor. Soc., 123, 467–489, https://doi.org/10.1002/qj.49712353811, 1997.

Wilhelm, L., Schwierz, C., Schröer, K., Taszarek, M., and Martius, O.: A Modelled Multi-Decadal Hailday Time Series for Switzerland, EGUsphere [preprint], https://doi.org/10.5194/egusphere-2024-371, 2024.

Zhou, Z., Zhang, Q., Allen, J. T., Ni, X., and Ng, C.-P.: How Many Types of Severe Hailstorm Environments Are There Globally?, Geophys. Res. Lett., 48, e2021GL095 485, https://doi.org/10.1029/2021GL095485, 2021.